



HAL
open science

Effect of meteoric ions on ionospheric conductance at Jupiter

Yuki Nakamura, Koichiro Terada, Chihiro Tao, Naoki Terada, Yasumasa Kasaba, François Leblanc, Hajime Kita, Aoi Nakamizo, Akimasa Yoshikawa, Shinichi Ohtani, et al.

► **To cite this version:**

Yuki Nakamura, Koichiro Terada, Chihiro Tao, Naoki Terada, Yasumasa Kasaba, et al.. Effect of meteoric ions on ionospheric conductance at Jupiter. *Journal of Geophysical Research Space Physics*, 2022, 127 (3), pp.e2022JA030312. 10.1029/2022JA030312 . insu-03613864

HAL Id: insu-03613864

<https://insu.hal.science/insu-03613864>

Submitted on 18 Aug 2022

HAL is a multi-disciplinary open access archive for the deposit and dissemination of scientific research documents, whether they are published or not. The documents may come from teaching and research institutions in France or abroad, or from public or private research centers.

L'archive ouverte pluridisciplinaire **HAL**, est destinée au dépôt et à la diffusion de documents scientifiques de niveau recherche, publiés ou non, émanant des établissements d'enseignement et de recherche français ou étrangers, des laboratoires publics ou privés.

Copyright

JGR Space Physics

RESEARCH ARTICLE

10.1029/2022JA030312

Key Points:

- Meteoric ions dominate the Jovian lower ionosphere due to their long lifetimes
- Pedersen and Hall conductances are enhanced, and they are independent of local time due to the large concentrations of meteoric ions
- The contribution of meteoric ions to conductance results from their large densities and altitudinal coincidence with the conductive layer

Correspondence to:


















Y. Nakamura,
yuki.nakamura.r2@dc.tohoku.ac.jp

Citation:

Nakamura, Y., Terada, K., Tao, C., Terada, N., Kasaba, Y., Leblanc, F., et al. (2022). Effect of meteoric ions on ionospheric conductance at Jupiter. *Journal of Geophysical Research: Space Physics*, 127, e2022JA030312. <https://doi.org/10.1029/2022JA030312>

Received 21 JAN 2022
Accepted 6 MAR 2022

Effect of Meteoric Ions on Ionospheric Conductance at Jupiter

Yuki Nakamura^{1,2} , Koichiro Terada¹, Chihiro Tao³ , Naoki Terada¹ , Yasumasa Kasaba¹ , François Leblanc² , Hajime Kita⁴ , Aoi Nakamizo³ , Akimasa Yoshikawa^{5,6} , Shinichi Ohtani⁷ , Fuminori Tsuchiya¹ , Masato Kagitani¹ , Takeshi Sakanoi¹ , Go Murakami⁸ , Kazuo Yoshioka⁹ , Tomoki Kimura¹⁰ , Atsushi Yamazaki⁸ , and Ichiro Yoshikawa⁹ 

¹Graduate School of Science, Tohoku University, Sendai, Japan, ²LATMOS/CNRS, Sorbonne Université, Paris, France,

³Space Environment Laboratory, National Institute of Information and Communications Technology (NICT), Koganei, Japan, ⁴Tohoku Institute of Technology, Sendai, Japan, ⁵International Center for Space Weather Science and Education,

Kyusyu University, Fukuoka, Japan, ⁶Department of Earth and Planetary Science, Kyushu University, Fukuoka, Japan, ⁷The Johns Hopkins University Applied Physics Laboratory, Laurel, MD, USA, ⁸Institute of Space and Astronautical Science, Japan Aerospace Exploration Agency, Sagami-hara, Japan, ⁹The University of Tokyo, Kashiwa, Japan, ¹⁰Tokyo University of Science, Tokyo, Japan

Abstract Ionospheric Pedersen and Hall conductances play significant roles in electromagnetic coupling between the planetary ionosphere and magnetosphere. Several observations and models have suggested the existence of meteoric ions with interplanetary origins in the lower part of Jupiter's ionosphere; however, no models have considered the contributions of meteoric ions to ionospheric conductance. This study is designed to evaluate the contribution of meteoric ions to ionospheric conductance by developing an ionospheric model combining a meteoroid ablation model and a photochemical model. We find that the largest contribution to Pedersen and Hall conductivities occurs in the meteoric ion layer at altitudes of 350–600 km due to the large concentration of meteoric ions resulting from their long lifetimes of more than 100 Jovian days. Pedersen and Hall conductances are enhanced by factors of 3 and 10, respectively, in the middle- and low-latitude and auroral regions when meteoric ions are included. The distribution of Pedersen and Hall conductances becomes axisymmetric in the middle- and low-latitude regions. Enhanced axisymmetric ionospheric conductance should impact magnetospheric plasma convection. The contribution of meteoric ions to the ionospheric conductance is expected to be important only on Jupiter in our solar system because of Jupiter's intense magnetic and gravitational fields.

1. Introduction

Ionospheric Pedersen and Hall conductances are important parameters controlling the ionospheric current, which serves to close the large-scale current circuit between the ionosphere and magnetosphere, and they play a significant role in the neutral dynamics of the thermosphere via Joule heating (e.g., Singhal, 1996; C. G. A. Smith et al., 2005). Previous numerical models of ionospheric conductance of Jupiter assumed that the ionosphere consists of H_3^+ , H^+ , and hydrocarbon ions, which originated from atmospheric molecules due to solar extreme ultraviolet (EUV) radiation in the nonauroral region and by electron precipitation in the auroral region (Gérard et al., 2020; Millward et al., 2002; Tao et al., 2009, 2010). In such an ionosphere, H_3^+ and hydrocarbon ions would make dominant contributions to the Pedersen conductance (Gérard et al., 2020; Tao et al., 2010). Accordingly, conductance differs significantly between the dayside and the nightside, leading to diurnal variations in the field-aligned current (FAC) density and magnetospheric plasma azimuthal velocity (Tao et al., 2010).

Ionospheric conductance depends strongly on the structure of the ionosphere, which, however, is poorly understood. The altitudinal profile of electron density has been measured by the radio occultation technique only a few times by the Voyager 1 and 2 spacecraft, Pioneer 10, and Galileo spacecraft (Fjeldbo et al., 1975; Hinson et al., 1997, 1998). Those measurements showed several peaks. The uppermost peak, 10^{11} m^{-3} at 1,700 km in altitude, is most likely associated with H^+ . The origin of the lowermost peak, 10^{11} m^{-3} at 500 km, is unknown. Kim and Fox (1994) tried to explain its origin in terms of hydrocarbon ions, but in their simulation, the concentration of hydrocarbon ions was 1 order of magnitude smaller than the observed concentration. The numerical model of Kim et al. (2001) reproduced the low-altitude electron density peak by considering the presence of metallic ions such as Mg^+ and Fe^+ with interplanetary origins, named meteoric ions. Hinson et al. (1998) suggested that

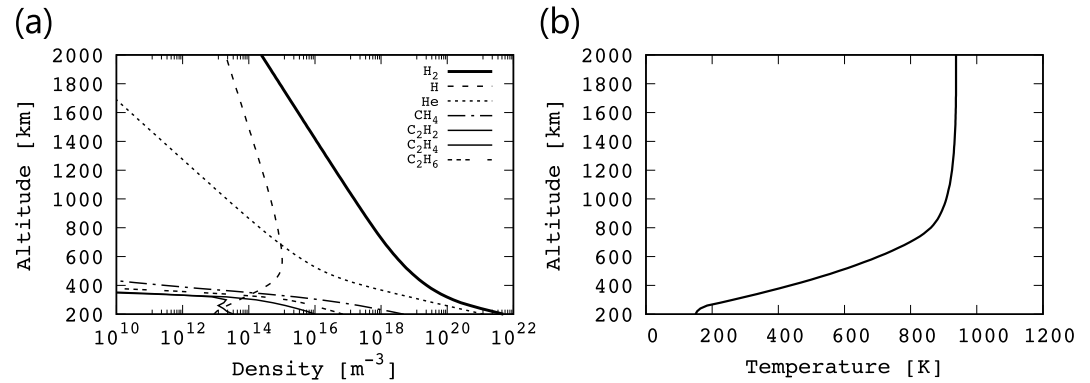


Figure 1. Vertical profiles of Jupiter's atmosphere used in our model. (a) Density of neutral atoms and molecules. (b) Temperature. Altitude is defined as the height above the 1 bar spheroid.

meteoric ions, if indeed they existed, could contribute to the Pedersen conductance, reaching up to 0.5 mho even in the nonauroral region. Thus, a large concentration of meteoric ions is suggested by both observations and numerical models.

In this study, we investigate the contributions of meteoric ions to the ionospheric conductance of Jupiter by using a newly developed Jovian ionosphere model, which couples a meteoroid ablation model and a photochemical model. In Section 2, we describe the numerical models used in this study. In Section 3, we describe the effects of meteoric ions on the ionospheric composition and ionospheric conductance. In Section 4, we discuss the factors leading to the contributions of meteoric ions to ionospheric conductances at Jupiter. Finally, conclusions are given in Section 5.

2. Model Description

2.1. Model Input

The neutral density and temperature profiles of Jupiter's atmosphere used in our model are shown in Figure 1. The density profiles of H₂ and He were derived from their scale heights, and those of CH₄, C₂H₂, C₂H₄, and C₂H₆ were taken from Moses and Poppe (2017). The density profile of H in Figure 1 was calculated self-consistently by a photochemical model. The temperature profile of the neutral atmosphere was taken from Grodent et al. (2001).

2.2. Meteoroid Ablation Model

We used a set of meteoroid ablation equations from Lebedinets et al. (1973). The interactions of small solid particles of interplanetary origin with planetary atmospheres can be described with the following system of differential equations. The equation of motion is

$$m \frac{dv}{dt} = -\Gamma \rho_a \pi r^2 v v + mg \quad (1)$$

where m is the mass of meteoroids, v is the velocity of meteoroids relative to the atmosphere, Γ is the frictional drag coefficient, ρ_a is the atmospheric mass density, r is the radius of meteoroids, and g is the gravitational acceleration. By defining that the x axis is horizontal and the z axis points vertically upward, Equation 1 can be divided into two components:

$$m \frac{dv_x}{dt} = -\Gamma \rho_a \pi r^2 v v_x \quad (2)$$

and

$$m \frac{dv_z}{dt} = -\Gamma \rho_a \pi r^2 v v_z - mg \quad (3)$$

Table 1
Parameters for the Meteoroid Ablation Model

Γ (frictional drag coefficient)	1.0	Hughes (1978)
Λ (heating efficiency)	1.0	Vondrak et al. (2008)
ϵ (emissivity)	1.0	Lebedinets et al. (1973)
Temperature of environment T_{eq}		Grodent et al. (2001)
Incident angle	45°	Hughes (1993)
Density of meteoroid ρ_a	1,200 kg m ⁻³	Kim et al. (2001)
Mass and velocity distribution of meteoroid		Moses and Poppe (2017)

The ablation equation is

$$\frac{dm}{dt} = -\Lambda_s \rho_a \pi r^2 \frac{v^3}{2Q} - \frac{4\pi r^2 C_1}{T^{1/2}} \exp(-C_2/T) \quad (4)$$

where Λ_s is the sputtering coefficient, T is the temperature of meteoroids, and the parameters $C_1 = 6.92 \times 10^{11}$ kg m⁻² s⁻¹ K^{-1/2} and $C_2 = 57,800$ K describe the dependence of evaporation rate on the temperature of the meteoroids. $Q = 7 \times 10^6$ J kg⁻¹ is the energy required for evaporation of 1 g of meteor substance (Lebedinets et al., 1973). The energy equation is

$$\frac{dT}{dt} = \frac{4\pi r^2}{c_{sh}m} \left[\frac{\Lambda - \Lambda_s}{8} \rho_a v^3 - \sigma \epsilon (T^4 - T_{eq}^4) - \frac{QC_1}{T^{1/2}} \exp(-C_2/T) \right] \quad (5)$$

where Λ is the heat transfer coefficient, Λ_s is the sputtering coefficient, $\sigma = 5.67 \times 10^{-8}$ J m⁻² s⁻¹ K⁻⁴ is the Stefan–Boltzmann constant, $\epsilon = 1$ is the radiative efficiency of the meteoroid, T_{eq} is the equilibrium temperature of the ambient environment, and $c_{sh} = 1 \times 10^3$ J kg⁻¹ K⁻¹ is the specific heat at constant density (Pesnell & Grebowsky, 2000). The sputtering coefficient Λ_s is determined by $\Lambda_s/Q = 10^{-16} \exp(T/290)$ (Lebedinets et al., 1973). The parameters of the meteoroid ablation model are listed in Table 1.

A fourth-order Runge–Kutta method was used for solving the system of differential Equations 2–5.

2.3. Photochemical Model and Conductivity

The photochemical model used in this study considered 406 neutral-ion chemical reactions for 55 ion species (H_2^+ , H^+ , H_3^+ , He^+ , HeH^+ , C^+ , CH^+ , CH_2^+ , CH_3^+ , CH_4^+ , CH_5^+ , C_2^+ , C_2H^+ , $C_2H_2^+$, $C_2H_3^+$, $C_2H_4^+$, $C_2H_5^+$, $C_2H_6^+$, $C_2H_7^+$, C_3H^+ , $C_3H_2^+$, $C_3H_3^+$, $C_3H_4^+$, $C_3H_5^+$, $C_3H_6^+$, $C_3H_7^+$, $C_3H_8^+$, $C_3H_9^+$, C_4H^+ , $C_4H_2^+$, $C_4H_3^+$, $C_4H_5^+$, $C_4H_7^+$, $C_4H_9^+$, Na^+ , NaH_2^+ , $NaCH_4^+$, $NaC_2H_2^+$, $NaC_2H_4^+$, Fe^+ , FeH^+ , FeH_2^+ , $FeCH_4^+$, $FeC_2H_2^+$, $FeC_2H_4^+$, Mg^+ , MgH^+ , MgH_2^+ , $MgCH_4^+$, $MgC_2H_2^+$, $MgC_2H_4^+$, Si^+ , SiH^+ , SiH_2^+ , and $SiC_nH_m^+$), the electron, 11 neutrals (H, CH_2 , CH_3 , Na, NaH, Fe, FeH, Mg, MgH, Si, and SiH), and 8 fixed neutrals (H_2 , H_2 ($\nu \geq 2$), H_2 ($\nu \geq 4$), He, CH_4 , C_2H_2 , C_2H_4 , and C_2H_6). All 406 chemical reactions considered in this study were taken from Kim and Fox (1994) and Kim et al. (2001), who described the important chemistry in Jupiter’s ionosphere, including that of hydrocarbon ions and meteoric ions. The list of reactions is found in Tables A1 and A2 in Appendix A. The dominant chemical pathways for hydrocarbon ions and meteoric ions are shown in Figure 6 of Kim and Fox (1994) and Figures 4–8 of Kim et al. (2001), respectively. The density profiles of vibrationally excited H_2 ($\nu \geq 2$) and H_2 ($\nu \geq 4$) were taken from Majeed and McConnell (1991). We used the EUVAC model for the solar EUV flux (Richards et al., 1994). F10.7 is assumed to be 140 as a moderate solar condition.

The photochemical model solves the following system of continuity equations for all species by using an implicit method:

$$\frac{\partial n_i}{\partial t} = P_i - L_i - \frac{\partial \Phi_i}{\partial z} \quad (6)$$

where n_i is the number density of the i th species, P_i is the production rate of the i th species, L_i is the loss rate of the i th species, and Φ_i is the flux of the i th species. The flux Φ_i for ions can be described as follows:

$$\Phi_i = -n_i D_i \left[\frac{1}{n_i} \frac{\partial n_i}{\partial z} + \frac{1}{H_i} + \frac{T_e/T_i}{P_e} \frac{\partial P_e}{\partial z} + \frac{1 + \alpha_i}{T_i} \frac{\partial T_i}{\partial z} \right] \quad (7)$$

where D_i is the binary diffusion coefficient of the i th species, $H_i = k_B T_i / m_i g$ is the scale height of the i th species, m_i is the mass of the i th species, k_B is the Boltzmann constant, T_e and T_i are the temperatures of the electron and of the i th species, respectively, $P_e = n_e k_B T_e$ is the electron pressure, n_e is the electron density, and α_i is the thermal diffusion coefficient. The thermal diffusion coefficient for H was taken from Hunten (1973) and those for other species were assumed to be zero. The binary diffusion coefficient D_i was calculated from

$$D_i = \frac{k_B T_i}{m_i \nu_{i-H_2}} \quad (8)$$

where ν_{i-H_2} is the frequency of binary collisions between the i th species and H_2 given by

$$\nu_{i-H_2} = 2n_{H_2} r^2 \left(\frac{2\pi k_B T (m_i + m_{H_2})}{m_i m_{H_2}} \right) \quad (9)$$

where n_{H_2} is the number density of H_2 , $r = 2.7 \times 10^{-10}$ m is the collision radius of H_2 , T is the neutral temperature, and m_i and m_{H_2} are the masses of the i th species and H_2 (Chapman & Cowling, 1970). Calculation by Nagy et al. (1976) showed that the electron temperature in the Jovian ionosphere follows the neutral temperature up to 1,500–2,000 km when the neutral temperature is about 1000 K at high altitudes. They showed that the electron temperature slowly increases with altitudes above 1,500–2,000 km but it increases only up to 1.1–1.4 times the neutral temperature even at 3,000 km. In this study, the temperatures of electrons and all other species were assumed to be the same as the neutral temperature between the model altitude range 200–3,000 km. The third term in Equation 7 is the ambipolar diffusion term described by the electron pressure gradient, which was applied only to ions. The electron density was determined by assuming charge neutrality.

For the auroral region, we took into account ionization of atmospheric hydrogen molecules caused by precipitation of auroral electrons. The altitude profile of the ionization rate for hydrogen molecules due to the impact by precipitating auroral electrons was calculated by using the parameterized equations obtained by Hiraki and Tao (2008). We applied the energy flux of precipitating electrons as a function of the FAC intensity presented by Nichols and Cowley (2004). We assumed that the electron velocity distribution was isotropic over the downward hemisphere at the top of the ionosphere. The electron velocity distribution is given by the following function:

$$f(v) = \frac{f_0}{\left(\frac{v}{v_0}\right)^\alpha + \left(\frac{v}{v_0}\right)^\beta} \quad (10)$$

where f_0 is a normalization constant, v is the velocity of precipitating electrons, α and β are the spectral slopes corresponding to the velocity ranges $v < v_0$ and $v > v_0$ if β is greater than α , respectively, and v_0 is the characteristic velocity. We applied $\alpha = 2$ and $\beta = 8$ in this study, as did Nichols and Cowley (2004) and Tao et al. (2009). f_0 and v_0 are given by

$$f_0 = \frac{j_{||i}}{\pi q_e} / \int_0^\infty \frac{v^3}{\left(\frac{v}{v_0}\right)^\alpha + \left(\frac{v}{v_0}\right)^\beta} dv \quad (11)$$

and

$$v_0 = \sqrt{\frac{2q_e \Phi}{m_e}} = \sqrt{\frac{2W_{th}}{m_e} \left(\frac{j_{||i}}{j_{||i0}} - 1 \right)} \quad (12)$$

where $j_{||i}$ is the FAC density in the ionosphere, $j_{||i0} = 0.0134 \mu A m^{-2}$ is the FAC density without electron acceleration, q_e is the elementary charge, Φ is the field-aligned voltage, and $W_{th} = 2.5$ keV is the thermal energy of the magnetospheric electrons. The FAC density distribution was calculated with the model described by Tao et al. (2009).

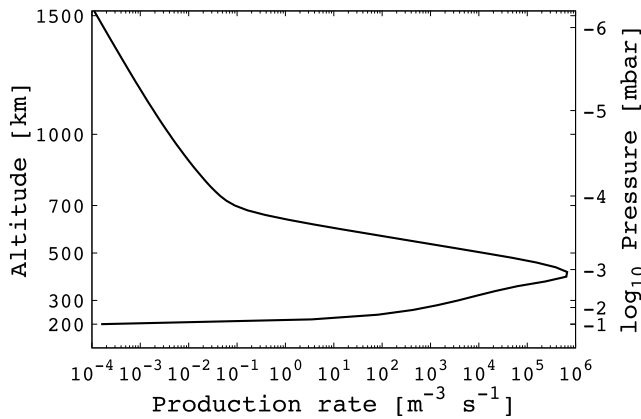


Figure 2. Sum of the production rates of metallic atoms (Fe, Mg, Si, and Na) and ions (Fe⁺, Mg⁺, Si⁺, and Na⁺) calculated by the meteoroid ablation model. The corresponding atmospheric pressure is shown on the vertical axis on the right side.

Pedersen conductivity σ_P and Hall conductivity σ_H are calculated using the following formulas:

$$\sigma_P = \frac{q_e n_e}{B} \left(\frac{\omega_e v_{e-H_2}}{v_{e-H_2}^2 + \omega_e^2} + \sum_i \frac{n_i}{n_e} \frac{\omega_i v_{i-H_2}}{v_{i-H_2}^2 + \omega_i^2} \right) \quad (13)$$

and

$$\sigma_H = \frac{q_e n_e}{B} \left(\frac{\omega_e^2}{v_{e-H_2}^2 + \omega_e^2} - \sum_i \frac{n_i}{n_e} \frac{\omega_i^2}{v_{i-H_2}^2 + \omega_i^2} \right) \quad (14)$$

where q_e is the elementary charge, B is the magnetic field strength, ω_e and ω_i are the cyclotron frequencies of the electron and the i th ion species, and v_{e-H_2} and v_{i-H_2} are the frequencies of binary collision between the electron and H₂, and between and the i th ion species and H₂, respectively. The magnetic field of Jupiter was assumed to be an axisymmetric dipole and was set to 4.28 G at the equatorial surface (Kivelson & Bagenal, 2007). v_{i-H_2} is already expressed as Equation 9, and v_{e-H_2} is expressed in the following equation (Chapman & Cowling, 1970):

$$v_{e-H_2} = n_{H_2} a_0^2 \left(\frac{2k_B \times 11600}{m_e} \right)^{1/2} \times (-0.0189T^{4.5} + 0.5354T^{3.5} - 5.5138T^{2.5} + 21.133T^{1.5} + 29.475T^{0.5}) \quad (15)$$

where a_0 is the Bohr radius, m_e is the mass of an electron, and T is the temperature in units of eV.

The horizontal resolution used in the model was 1° in longitude and 1° in latitude, and the vertical resolution used in the model was 20 km in the altitude range 200–3,000 km. By neglecting horizontal transport of atmospheric constituents except for rotation, the calculation of the photochemical model was performed in two steps: (a) stable solution and (b) rotational solution. In the stable solution, the local time (LT) was fixed at 12:00 LT at all latitudes, and the solar flux was set to be half of its flux at 12:00 LT as the diurnal mean solar flux. The stable solution was obtained after an integration time corresponding to 1,000 Jupiter days. In the rotational solution, the result from the stable solution was used as the initial density. The calculation started from 12:00 LT meridian grids. The ion and electron densities were transferred to the next grid when the integration time reached 1/360 of a Jovian day (1 longitudinal grid). In the rotational solution, we ran the calculation over 2.5 Jupiter days to obtain a quasi steady state solution. The transport of solar flux near the terminator was treated by the equation taken from F. L. Smith and Smith (1972) with the improved approximation of complementary error functions from Ren and ManKenzie (2007).

3. Results

3.1. Production Rate of Meteoric Species

The mass and velocity distributions of the incident meteoroids on Jupiter were taken from Moses and Poppe (2017). The element composition of the meteoroids was assumed to be CI chondrite (Kim et al., 2001), in which the elements are Fe, Mg, Si, and Na with mass fractions of 19.0%, 9.9%, 10.6%, and 0.5%, respectively. Meteoric atoms ablated from the surface of the meteoroid collide with atmospheric molecules and are ionized to form meteoric ions. The ionization probability during this process depends on the entry velocity of meteoroids (Lebedinets et al., 1973), and it has been estimated to be 0.4 at Jupiter (Kim et al., 2001). The time scale for condensation of metallic atoms is assumed to be 10⁵ s, which is the shortest case estimated by Moses and Bass (2000) for the atmosphere of Saturn; this was used here to avoid overestimating the concentration of metallic species.

Figure 2 shows the sum of the production rates for all meteoric atoms (Fe, Mg, Si, and Na) and ions (Fe⁺, Mg⁺, Si⁺, and Na⁺) calculated by the meteoroid ablation model. The peak production rate was $\sim 7 \times 10^5 \text{ m}^{-3} \text{ s}^{-1}$ at an atmospheric pressure of 10⁻³ mbar, which is in good agreement with the peak deposition rate for silicate grains calculated by Moses and Poppe (2017) in terms of both intensity and pressure level. The sum of the production rates of all meteoric atoms and ions calculated by our meteoroid ablation model was larger than the production

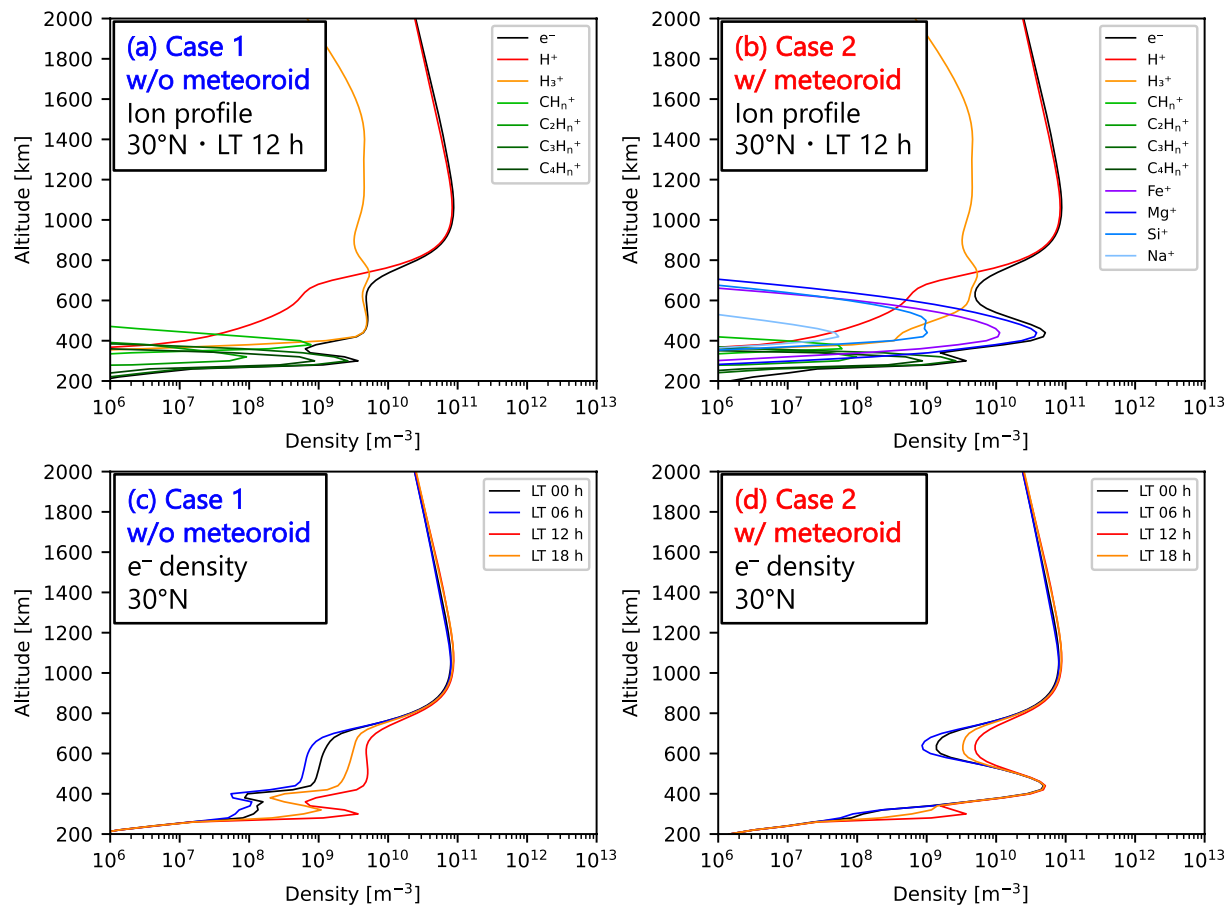


Figure 3. (a, b) Calculated ion density profiles at 30°N and 12:00 local time (LT) for Case 1 and Case 2, respectively. (c, d) Local time dependence of electron density as a function of altitude in Case 1 and Case 2, respectively. Black, blue, red, and orange solid curves represent the profiles at 0:00 LT, 6:00 LT, 12:00 LT, and 18:00 LT, respectively.

rate for silicate grains calculated by Moses and Poppe (2017) at pressure levels lower than 10^{-4} mbar. This discrepancy came from the different treatments of sputtering, which is the dominant mass loss process at high altitudes. Sputtering is the dominant mass loss process for meteoroids before the temperature of the meteoroid becomes high enough to cause evaporation. Moses and Poppe (2017) assumed that the effects of sputtering were negligibly small, whereas our model includes the sputtering term. Since the production rate of meteoric atoms and ions above an altitude corresponding to an atmospheric pressure of 10^{-4} mbar is 8 orders of magnitude smaller than the peak value, such a high-altitude region is not important for ionospheric chemistry.

3.2. Ion and Electron Density Profiles

To evaluate the effects of meteoric ions on the ionosphere of Jupiter, we calculated two cases for the ionosphere: Case 1 is the ionosphere without meteoroid influx, and Case 2 is the ionosphere with meteoroid influx. In Case 2, we used the production rate of meteoric atoms and ions calculated with the meteoroid ablation model (Section 3.1). We ran our model over 1,000 Jovian days to obtain a steady solution at noon. After reaching a steady solution, we ran the model with planetary rotation over 2.5 Jupiter days and the meteoroid influx was assumed to be 9 times larger on the leading hemisphere (00:00 LT ~ 12:00 LT) than on the trailing hemisphere (12:00 LT ~ 24:00 LT).

Figure 3 shows the density profiles of ions and electrons in (a) Case 1 and (b) Case 2 at the latitude of 30°N and a LT of 12:00. In Case 1, H⁺ was dominant above an altitude of 750 km with a peak density of 10^{11} m⁻³, H₃⁺ was dominant in the altitude range between 400 and 700 km with a peak density of approximately 5×10^9 m⁻³, and hydrocarbon ions were dominant below 400 km altitude with a peak density of approximately 5×10^9 m⁻³.

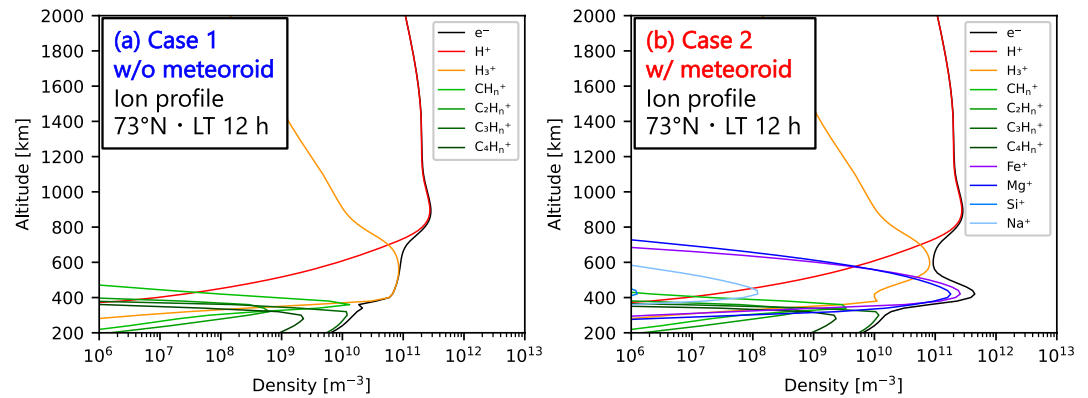


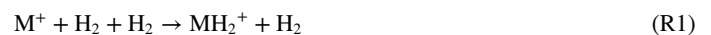
Figure 4. Calculated ion density profiles in Case 1 (a) and Case 2 (b) at 73°N and 12:00 LT. Symbols are defined as in Figure 3.

The structure of the ion composition in Case 1 agreed well with the results of Kim and Fox (1994). In Case 2, the ion density profile above 600 km was almost the same as that in Case 1. The profile was different below 600 km due to the presence of meteoric species. An additional peak appeared at an altitude of 420 km with a density of $5 \times 10^{10} \text{ m}^{-3}$. The dominant ions in the meteoric ion layer were Mg^+ and Fe^+ . The densities of H_3^+ and CH_n^+ were depleted at altitudes between 350 and 600 km due to charge exchange with meteoric atoms. The altitudes and densities of the meteoric ions were in good agreement with those of Kim et al. (2001).

The dependence of the electron density at a latitude of 30°N on LT in Case 1 and Case 2 is shown in Figures 3c and 3d, respectively. In both cases, there was no clear LT dependence above 800 km, where H^+ was dominant. In Case 1, the electron density distribution showed a clear LT dependence below 700 km, where molecule ions such as H_3^+ and hydrocarbon ions were dominant. At this altitude range, the electron density increased at noon due to photoionization of ambient neutral molecules by solar EUV irradiation and effectively decreased on the nightside from dusk to dawn due to dissociative recombination of molecular ions and electrons. In Case 2, the LT variation of the electron density was seen only in the altitude range between 500 and 700 km, where H_3^+ was dominant. In the altitude range between 350 and 500 km, there was no apparent LT dependence, especially in the meteoric ion layer.

Figure 4 shows the density profiles of ions and electrons in (a) Case 1 and (b) Case 2 in the auroral region at the latitude of 73°N and a LT of 12:00. In the auroral region, meteoric ions were dominant in the altitude range between 350 and 600 km, as well as in the middle latitudes shown in Figure 3. Compared with the middle-latitude region, the peak density of the meteoric ion was enhanced by 1 order of magnitude in the auroral region because of the charge exchange reaction between meteoric atoms and H_3^+ produced by precipitating auroral electrons. Note that the density profile in the auroral region strongly depends on the assumed energy flux of the precipitating electrons.

The lifetimes of meteoric ions are essential in understanding their large concentrations. The major loss processes for Mg^+ and Fe^+ (M^+ , hereafter), which are the primary ions in the meteoric ion layer, are three-body adduct reactions with H_2 to form MH_2^+ . However, the adduct reaction does not contribute to the net loss of M^+ because the M^+ density is balanced by the following sequence of reactions after the adduct reaction.



and



The pathway for this process, as suggested by Lyons (1995) and Kim et al. (2001), is as follows. (R1) M^+ is effectively removed from the ionosphere by a three-body adduct reaction with H_2 to produce MH_2^+ . (R2) MH_2^+ subsequently reacts with ambient H to produce MH^+ metal hydride ions. (R3) The metal hydride ion MH^+ reacts

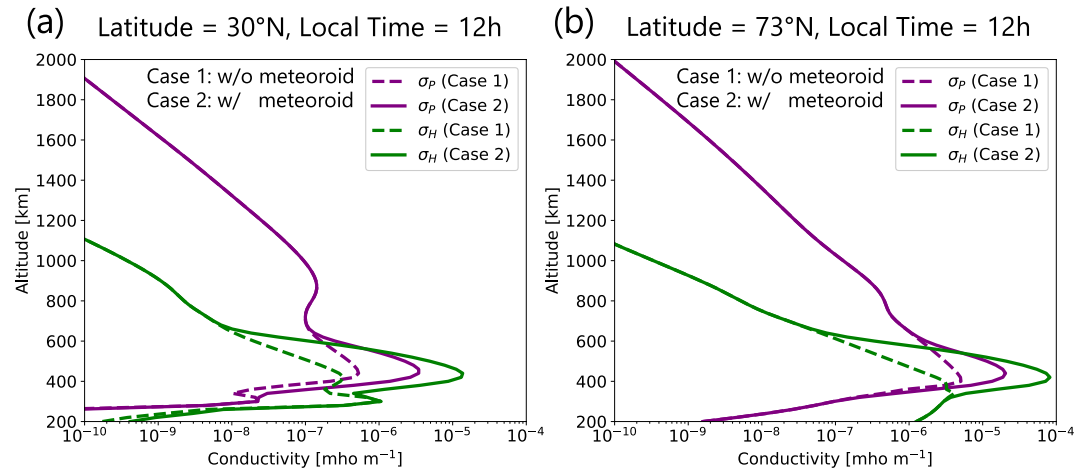
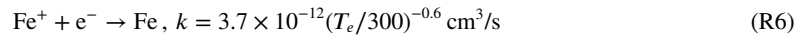
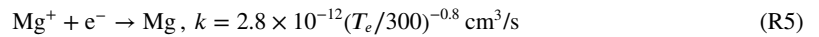


Figure 5. (a) Pedersen and Hall conductivity profiles at a latitude of 30°N and a local time of 12:00 and (b) in the auroral region at a latitude of 73°N and a local time of 12:00. Purple curves show Pedersen conductivity profiles, and green curves show Hall conductivity profiles. Dashed curves show the conductivity profiles in Case 1, and solid curves show the conductivity profiles in Case 2.

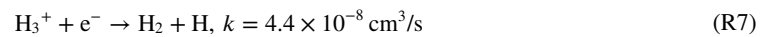
again with H to reform M^+ . Since the adduct reaction does not constitute a net loss of M^+ , the net loss of M^+ is caused by radiative recombination with electrons.



The reaction rate coefficient for radiative recombination of atomic ions with electrons is 4 orders of magnitude smaller than that for dissociative recombination of molecular ions with electrons.



and



By using the reaction rate coefficient k and electron density $[e^-]$, the lifetime of ions can be estimated as $1/k [e^-]$ for the major ions. In the following estimation of ion lifetimes, the electron temperature T_e was set to 600 K at 500 km where H_3^+ and meteoric ions dominate the ionosphere in Case 1 and Case 2, respectively, based on the assumption that the electron temperature is equal to the neutral temperature as already mentioned in Section 2.2. The electron density was equal to $5 \times 10^9 \text{ m}^{-3}$ at the altitude where H_3^+ density peaks in Case 1 at middle latitudes. The lifetime of H_3^+ was approximately 4,000 s. The electron density was equal to $5 \times 10^{10} \text{ m}^{-3}$ at the altitude where meteoric ions peak in Case 2 at middle latitudes. The lifetime of Mg^+ was 1×10^7 s and that of Fe^+ was 8×10^6 s, both of which are on the order of 300 Jovian days. The lifetime of meteoric ions was long enough to maintain their density even if the meteoroid influx is set to be asymmetric in LT.

3.3. Ionospheric Conductivity

We calculated ionospheric Hall and Pedersen conductivities by using the ions and electron density distributions calculated with the photochemical model. Figure 5a shows the Pedersen (purple lines) and Hall (green lines) conductivity profiles in Case 1 (dashed lines) and Case 2 (solid lines) at a latitude of 30°N and at a LT of 12:00. In Case 1, the peak altitude for the Pedersen conductivity was 420 km with a maximum value of $5 \times 10^{-7} \text{ mho m}^{-1}$, and the peak altitude of the Hall conductivity was 300 km with a maximum value of $1 \times 10^{-6} \text{ mho m}^{-1}$. In Case 2, both Hall and Pedersen conductivities peaked at 420 km at the altitude of the meteoric ion layer. The maximum values of the Pedersen and Hall conductivities in Case 2 were 3×10^{-6} and $1 \times 10^{-5} \text{ mho m}^{-1}$, respectively, which are 6 and 10 times larger than the values in Case 1, respectively. Figure 5b shows the Pedersen (purple lines) and

Hall (green lines) conductivity profiles in Case 1 (dashed lines) and Case 2 (solid lines) in the auroral region at 73°N and 12:00 LT. Here, again, both Pedersen and Hall conductivities peaked at the altitude of the meteoric ion layer in Case 2. The maximum values of Pedersen and Hall conductivities were enhanced by factors of 3 and 10 with respect to Case 1, respectively.

Figure 6 shows the global distribution for height-integrated Pedersen and Hall conductivities (defined as Pedersen and Hall conductances hereafter), respectively, in Case 1 (a and b) and in Case 2 (c and d). Pedersen and Hall conductances as a function of colatitude are shown in Figures 6e and 6f. In Case 1, both Pedersen and Hall conductance distributions showed clear LT variations in the middle- and low latitudes. At a latitude of 30°N, the Pedersen conductance was 0.14 mho at noon and 0.054 mho at midnight, and the Hall conductance was 0.088 mho at noon and 0.010 mho at midnight. The magnitudes of both the Pedersen and Hall conductances were larger on the dayside than on the nightside due to larger ion and electron concentrations. In the auroral region, the Pedersen conductance was 1.0 mho, and the Hall conductance was 0.76 mho. In Case 2, neither the Pedersen nor Hall conductance distributions showed a LT dependence and became quasi-axisymmetric in the middle and low latitudes. At a latitude of 30°N, the Pedersen conductance was 0.48 mho at noon and 0.42 mho at midnight, and the Hall conductance was 1.44 mho at noon and 1.33 mho at midnight. In the auroral region, the Pedersen conductance was 2.8 mho, and the Hall conductance was 8.8 mho. The magnitude of the Pedersen conductance was enhanced by a factor of 3 in the dayside middle-latitude and in the auroral region. The magnitude of the Hall conductance was enhanced by a factor of 10 in the dayside middle-latitude and auroral region. In the nightside middle-latitude region, the Pedersen conductance was enhanced by a factor of 8, and the Hall conductance was enhanced by a factor of 100. These results were due to the large contributions of long-lived meteoric ions to the both Pedersen and Hall conductances in Case 2.

We examined the sensitivity of the ionospheric conductance enhancement to meteoroid influx. Figure 7 shows the dependence of the ratios of (a) Pedersen conductance enhancement and (b) Hall conductance enhancement on meteoroid influx. In both middle-latitudes and auroral regions, the magnitudes of the Pedersen and Hall conductances increased by a factor of 3 when the meteoroid influx increased by a factor of 10. As mentioned before, the net loss process for meteoric ions is radiative recombination with electrons. By defining $[M^+]$ as the density of meteoric ions, $P(M^+)$ as the production rate of meteoric ions due to meteoroid ablation, and k as the reaction rate coefficient for radiative recombination with electrons, the following continuity equation was satisfied in the steady state:

$$P(M^+) - k[M^+][e^-] = 0 \quad (16)$$

If a meteoric ion M^+ is the major ion, the electron density $[e^-]$ is equal to $[M^+]$ if charge neutrality is assumed, and then the density of meteoric ions $[M^+]$ is proportional to $\sqrt{P(M^+)}$, where $P(M^+)$ is proportional to meteoroid influx. Since there is a large contribution from meteoric ions to ionospheric conductances, ionospheric conductances are nearly proportional to the concentration of meteoric ions, which is proportional to the square root of the meteoroid influx.

4. Discussion

We have shown that meteoric ions contribute significantly to the ionospheric conductivities at Jupiter, whereas it is known that meteoric ions do not contribute to the ionospheric conductivities at Earth. Why do meteoric ions contribute at Jupiter? There are two reasons.

The first reason is Jupiter's intense surface magnetic field. The conductive layer of the ionosphere is located in the region where the cyclotron frequency of ions is less than the frequency of ion collisions with atmospheric molecules and the cyclotron frequency of electrons is larger than the frequency of electron collisions with atmospheric molecules. The surface magnetic field on Jupiter is 15 times stronger than that on Earth. Cyclotron frequencies of ions and electrons are proportional to the strength of the local magnetic field. A strong magnetic field causes larger cyclotron frequencies, which implies that a denser and lower ionosphere will contribute more significantly to ionospheric Hall and Pedersen conductivities. A schematic illustration of the meteoric ion layer and conductive layer is shown in Figure 8. On Earth, the conductive layer is far above the meteoric ion layer. Due to the stronger magnetic field at Jupiter, the conductive layer corresponds to a larger atmospheric density and partially overlaps the meteoric ion layer.

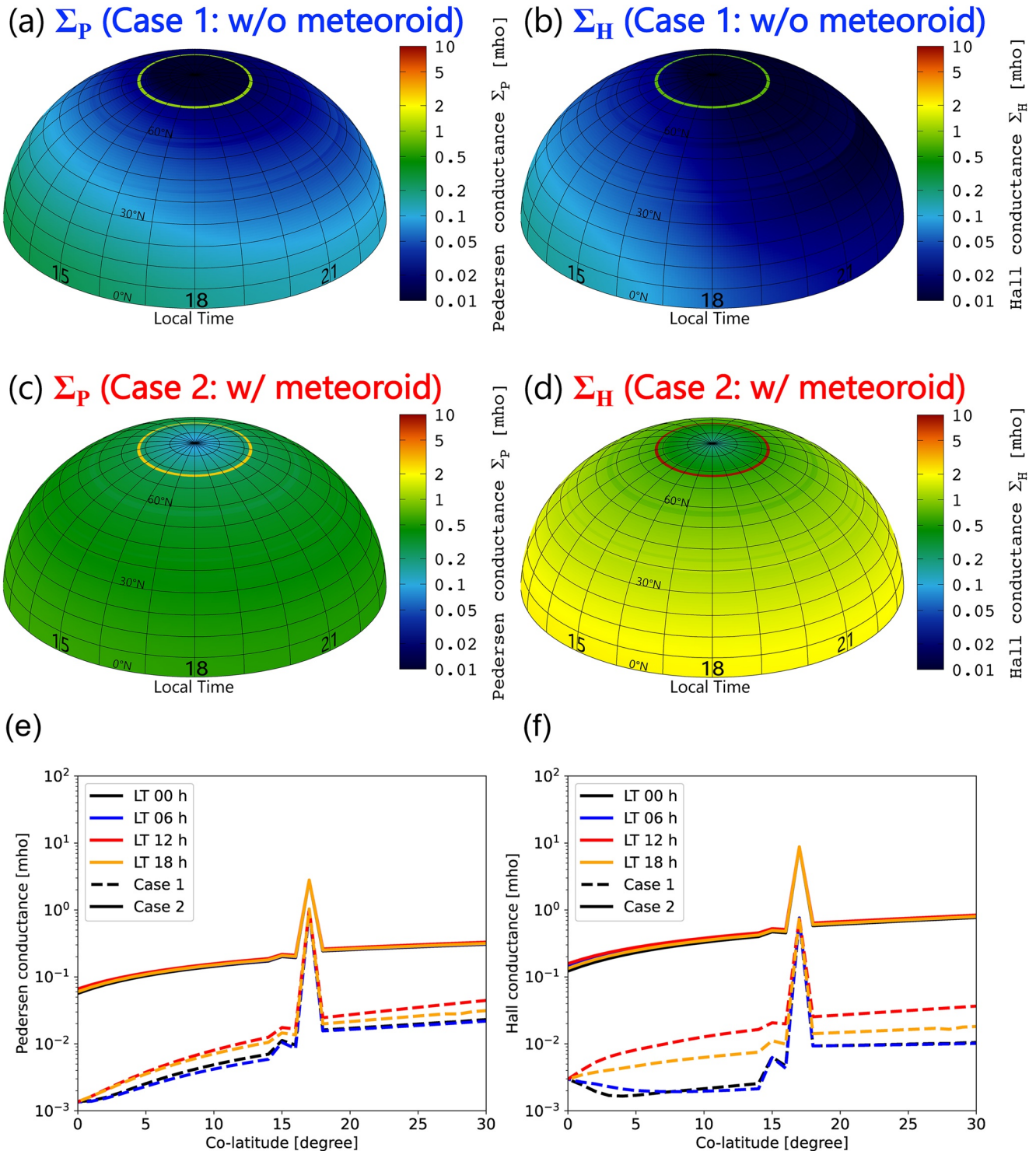


Figure 6. (a, b) Global distributions of calculated height-integrated Pedersen conductivity (Pedersen conductance, Σ_P) and height-integrated Hall conductivity (Hall conductance, Σ_H) in Case 1. (c, d) Global distribution of the calculated Σ_P and Σ_H in Case 2. Color bars represent conductance in units of mho. (e, f) The calculated Σ_P and Σ_H as a function of colatitude, respectively. Dashed lines show the calculated conductances in Case 1 and solid lines show those in Case 2. Black, blue, red, and orange lines in both Case 1 and Case 2 represent the conductances at 0:00 LT, 6:00 LT, 12:00 LT, and 18:00 LT, respectively.

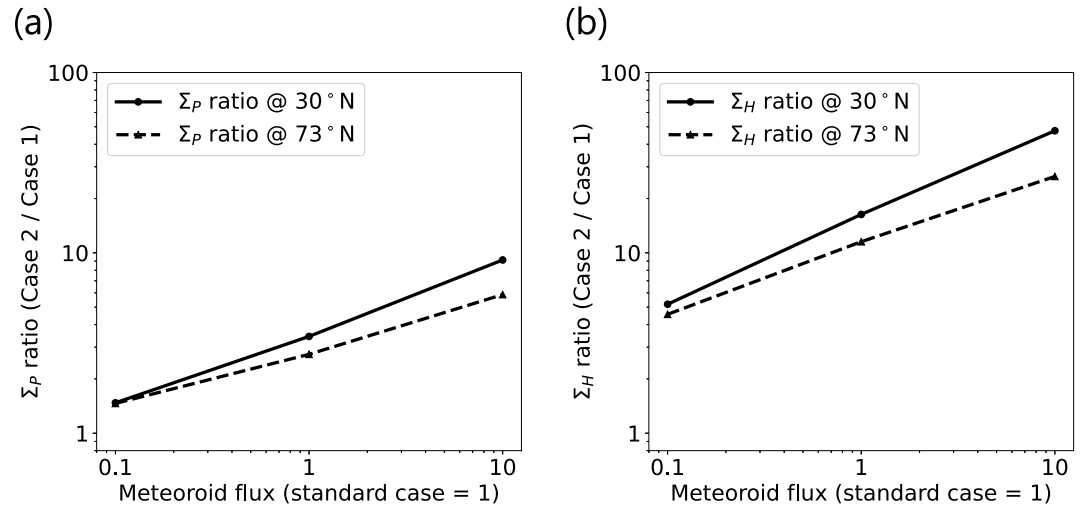


Figure 7. (a, b) Dependence of Pedersen and Hall conductances on meteoroid flux, respectively. We displayed the ratios for the ionospheric conductances between Case 2 and Case 1. Solid lines show this ratio at a latitude of 30°N and a local time of 12:00, and dashed lines show this ratio in the auroral region at a latitude of 73°N and a local time of 12:00.

We investigated the dependence of ionospheric conductance enhancement on the magnetic field strength. Figure 9a shows the dependence of the enhancement ratio for Pedersen conductance in Case 2 to that for Case 1 on magnetic field strength.

The magnetic field strength was changed in both Case 1 and Case 2, and other parameters, such as meteoric input and atmospheric conditions, were the same as those in the previous calculation shown in Figure 6. The magnetic field strengths of various planets in our solar system are indicated on the horizontal axis (Kivelson & Bagenal, 2007). Meteoric ions do not contribute to the Pedersen conductance at magnetic field strengths less than 0.3 times that of Jupiter. The enhancement ratio of the Pedersen conductance was increased by a factor of 3 at the Jupiter magnetic field strength. The Pedersen conductance enhancement ratio was largest when the magnetic field strength reached a value 10 times larger than that of Jupiter. These trends were similar for middle-latitude and auroral regions. Meteoric ions are therefore not expected to contribute to the Pedersen conductance at planets in our solar system except for Jupiter. Figure 9b shows the dependence of the enhancement ratio for Hall conductance in Case 2 to that in Case 1 on magnetic field strength. The enhancement ratio of the Hall conductance was largest for a magnetic field strength equal to that of Jupiter. Here, again, the contribution of meteoric ions to the Hall conductance was less important at other planets than at Jupiter.

The second reason is Jupiter's gravity. The gravitational acceleration for Jupiter at the ionospheric altitude is $\sim 25 \text{ m s}^{-2}$, which is approximately 2.5 times larger than that of the Earth ($\sim 10 \text{ m s}^{-2}$). A stronger gravity field results in a faster entry speed for incident meteoroids. The mean entry speed of meteoroids is $\sim 10 \text{ km s}^{-1}$ on Earth and $\sim 60 \text{ km s}^{-1}$ on Jupiter (Nesvorný et al., 2010; Poppe, 2016). Since the ablation rate and the increase in temperature depend on v^3 (v is the velocity of the meteoroid with respect to the atmosphere, as seen in Equations 4 and 5), meteoroids are more efficiently heated at Jupiter than at the Earth. Taking into account the difference in meteoroid fluxes for Jupiter and the Earth as well as the difference in entry speeds, the ablation rate of meteoroids is 10 times larger on Jupiter than on Earth (Plane et al., 2018). Furthermore, the ionization probability of ablated

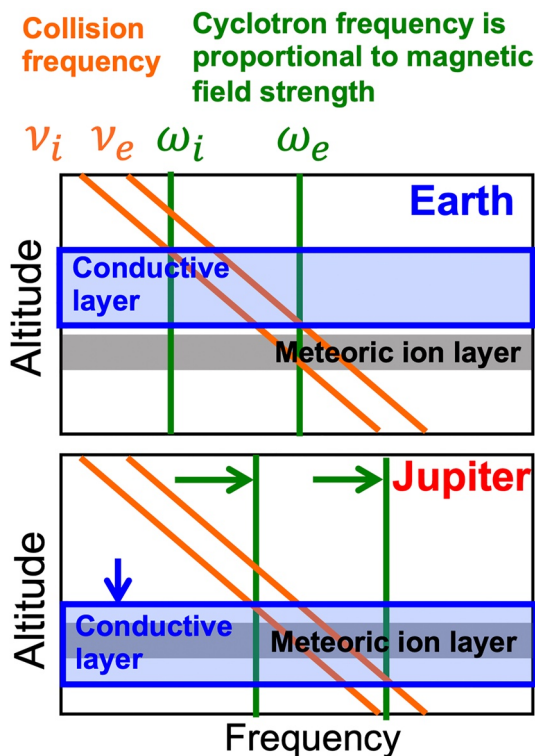


Figure 8. Schematic illustration of the conductive layers (blue rectangles) and meteoric ion layers (gray rectangles) of Earth and Jupiter. The conductive layer is the region where the conditions $\omega_i < \nu_i$ and $\omega_e > \nu_e$ are satisfied. ω_i and ω_e are the cyclotron frequencies of ions and electrons, and ν_i and ν_e are the frequencies for collision of ions and electrons with atmospheric molecules.

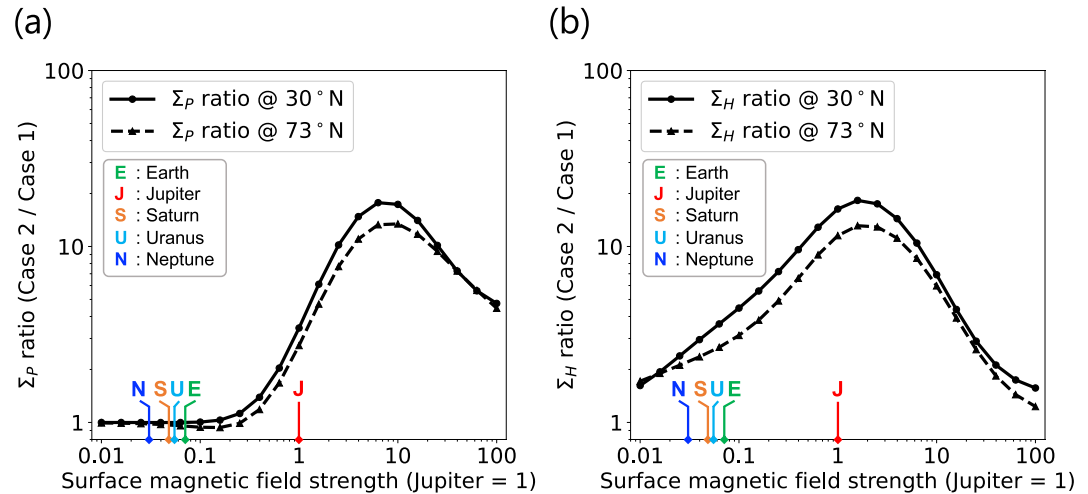


Figure 9. (a, b) Dependence of Pedersen and Hall conductances on the surface magnetic field strength, respectively. The ratio of ionospheric conductance is the ratio of the conductance in Case 2 to that in Case 1. The magnetic field strength is changed in both Case 1 and Case 2, and other parameters, such as meteoric input and atmospheric conditions, are the same as those of the previous calculation shown in Figure 6. Solid lines show this ratio at a latitude of 30°N and a local time of 12:00, and the dashed lines show this ratio in the auroral region at a latitude of 73°N and a local time of 12:00. The corresponding magnetic field strengths of planets in our solar system are indicated on the horizontal axis (the magnetic field strength of each planet was taken from Kivelson and Bagenal [2007]).

meteoric atoms is proportional to $v^{3.5}$ (Lebedinets et al., 1973). The faster entry speed on Jupiter relative to Earth results in more efficient direct ionization of meteoric substances.

Vertical neutral wind shear could temporarily enhance the concentration of meteoric ions. The sporadic E (E_s) layer is a temporary narrow layer on Earth with a large concentration of electron and metallic ions of interplanetary origin at altitudes between 90 and 120 km (Shinagawa et al., 2017). The E_s layer is formed by vertical neutral wind shear in the lower thermosphere, which originates from gravity and planetary waves that propagate from lower altitudes (Shinagawa et al., 2017). Numerical simulation by Barrow and Matcheva (2011) showed that the vertical shear in the background neutral wind induced by gravity waves can produce structured electron density layers at altitudes between 500 and 700 km at the Jovian ionosphere, which can explain sharp electron density peaks observed by radio occultation measurements by the Galileo satellite. Although they did not include meteoric ions in their calculations, it is expected that the gravity waves propagating at lower thermosphere of Jupiter can modify magnitudes and distributions of meteoric ions. If such a sporadic layer is also formed at Jupiter, it could be speculated that the ionospheric conductance is enhanced by the neutral wind shear in the lower thermosphere, and the distribution of ionospheric conductance could depend on the distribution of neutral wind in the lower thermosphere.

Enhanced ionospheric conductance due to meteoric ions is expected to affect plasma dynamics in the Jovian magnetosphere. Tao et al. (2010) suggested that diurnal variation in the ionospheric conductance leads to the diurnal variations in magnetospheric plasma azimuthal velocity. Our model showed that the ionospheric conductance becomes axisymmetric due to contributions from long-lived meteoric ions, which is expected to suppress such diurnal variation. Furthermore, enhanced Pedersen conductance due to meteoric ions could increase the azimuthal velocity of the magnetospheric plasma and FAC density.

5. Conclusions

In previous studies, Jupiter's ionospheric conductivity models and M-I coupling models considered the ionosphere to consist of ions originating from hydrogen and hydrocarbons. However, meteoric ions were also suggested to contribute to ionospheric conductance (Hinson et al., 1998). To clarify the effects of meteoric ions on Jupiter's ionospheric conductance, we developed a new Jovian ionospheric model by coupling meteoroid ablation and photochemical models.

In our Jovian ionospheric model, we evaluated two cases: Case 1 without meteoroid influx and Case 2 with meteoroid influx. In the middle-latitude region and in the auroral region, meteoric ions dominated the ionosphere at altitudes ranging between 350 and 600 km, so the densities of meteoric ions and of electrons do not vary with LT due to the long lifetimes of meteoric ions. By using the ion and electron density distributions, we evaluated the contribution of the meteoric ions to ionospheric conductances. In the middle- and low-latitude regions, the distributions of both the Pedersen and Hall conductances were enhanced and became axisymmetric due to the largest contribution from long-lived meteoric ions. In the auroral region, both Pedersen and Hall conductances were enhanced at nearly the same rate as in the middle-latitude region. Since the magnetic field of Jupiter was assumed to be an axisymmetric dipole and its axis aligned with rotational axis, the ionospheric conductance distribution exhibited axisymmetric with respect to the rotational axis. However, it is known that the magnetic field of Jupiter varies with longitudes and the axis of its dipole component tilts by 9.6° from the rotational axis (e.g., Acuna & Ness, 1976; Connerney et al., 2022). When a more realistic magnetic field configuration is applied, the ionospheric conductance distribution is not axisymmetric with respect to the rotational axis but should depend on longitudes due to the inhomogeneous magnetic field strength distribution. However, our conclusions that the ionospheric conductances are enhanced and their distributions are independent of LT by the presence of meteoric ions are unchanged regardless of this assumption.

Our results showed that meteoric ions contribute significantly to ionospheric conductance at Jupiter, whereas they are not known to contribute to conductance at Earth. Possible explanations for why meteoric ions contributed to ionospheric conductance are (a) Jupiter's intense surface magnetic field, which is a key factor causing coincidence in the altitude region between the conductive layer and the meteoric ion layer, and (b) Jupiter's intense gravity field, which is a key factor controlling the efficiency of meteoroid ablation and direct ionization of meteoric substances. Since the contributions of meteoric ions to ionospheric conductance are not expected at other planets in our solar system, their significance at Jupiter is of great importance in comparative planetology. Such enhanced axisymmetric ionospheric conductance is expected to modify magnetospheric plasma convection. Further modeling is needed to investigate the effects of meteoric ions on plasma dynamics, and further observations of the structures of the ionosphere, plasma velocity, and FAC are needed to confirm our results.

Appendix A

In this Appendix, chemical reactions used in the photochemical model are listed. Chemical reactions for hydrogen and hydrocarbon ions are listed in Table A1, which was used both in Case 1 and Case 2 calculations. Chemical reactions for meteoric ions are listed in Table A2, which was used only in Case 2 calculation.

Table A1 <i>Chemical Reaction List Considered in the Photochemical Model</i>				
Reaction			Rate coefficient	Reference
$\text{H}_2 + e^{-*}$	\rightarrow	$\text{H}_2^+ + e^- + e^{-*}$	Impact ionization	*
$\text{H} + h\nu$	\rightarrow	$\text{H}^+ + e^-$		a
$\text{H}_2 + h\nu$	\rightarrow	$\text{H}_2^+ + e^-$		a
$\text{H}_2 + h\nu$	\rightarrow	$\text{H}^+ + e^- + \text{H}$		a
$\text{He} + h\nu$	\rightarrow	$\text{He}^+ + e^-$		a
$\text{CH}_4 + h\nu$	\rightarrow	$\text{CH}_4^+ + e^-$		a
$\text{CH}_4 + h\nu$	\rightarrow	$\text{CH}_3^+ + e^- + \text{H}$		a
$\text{CH}_4 + h\nu$	\rightarrow	$\text{H}_2^+ + e^- + \text{products}$		a
$\text{C}_2\text{H}_2 + h\nu$	\rightarrow	$\text{C}_2\text{H}_2^+ + e^-$		b, c
$\text{C}_2\text{H}_4 + h\nu$	\rightarrow	$\text{C}_2\text{H}_4^+ + e^-$		d
$\text{C}_2\text{H}_4 + h\nu$	\rightarrow	$\text{C}_2\text{H}_3^+ + e^- + \text{H}$		d
$\text{C}_2\text{H}_4 + h\nu$	\rightarrow	$\text{C}_2\text{H}_2^+ + e^- + \text{products}$		d
$\text{C}_2\text{H}_4 + h\nu$	\rightarrow	$\text{C}_2\text{H}^+ + e^- + \text{products}$		d
$\text{C}_2\text{H}_6 + h\nu$	\rightarrow	$\text{C}_2\text{H}_6^+ + e^-$		e
$\text{C}_2\text{H}_6 + h\nu$	\rightarrow	$\text{C}_2\text{H}_5^+ + e^- + \text{H}$		e

Table A1
Continued

Reaction		Rate coefficient	Reference
$C_2H_6 + h\nu$	→	$C_2H_4^+ + e^- + \text{products}$	e
$C_2H_6 + h\nu$	→	$C_2H_3^+ + e^- + \text{products}$	e
$C_2H_6 + h\nu$	→	$C_2H_2^+ + e^- + \text{products}$	e
$H^+ + e^-$	→	H	$4.0 \times 10^{-12} \times (T_e/250.0)^{-0.7}$ 1
$He^+ + e^-$	→	He	$4.0 \times 10^{-12} \times (T_e/250.0)^{-0.7}$ 1
$HeH^+ + e^-$	→	H + He	$1.0 \times 10^{-8} \times (T_e/300.0)^{-0.6}$ 1
$H_2^+ + e^-$	→	H + H	$2.3 \times 10^{-7} \times (T_e/300.0)^{-0.4}$ 1
$H_3^+ + e^-$	→	$H_2 + H$	$4.4 \times 10^{-8} \times (T_e/300.0)^{-0.5}$ 1
$H_3^+ + e^-$	→	H + H + H	$5.6 \times 10^{-8} \times (T_e/300.0)^{-0.5}$ 1
$C^+ + e^-$	→	C	$4.0 \times 10^{-12} \times (T_e/250.0)^{-0.7}$ 1
$CH^+ + e^-$	→	C + H	$1.5 \times 10^{-7} \times (T_e/300.0)^{-0.42}$ 1
$CH_2^+ + e^-$	→	CH + H	$2.5 \times 10^{-7} \times (T_e/300.0)^{-0.5}$ 1
$CH_3^+ + e^-$	→	$CH_2 + H$	$3.5 \times 10^{-7} \times (T_e/300.0)^{-0.5}$ 1
$CH_4^+ + e^-$	→	$CH_3 + H$	$3.5 \times 10^{-7} \times (T_e/300.0)^{-0.5}$ 1
$CH_4^+ + e^-$	→	$CH_2 + H + H$	$3.5 \times 10^{-7} \times (T_e/300.0)^{-0.5}$ 1
$CH_5^+ + e^-$	→	$CH_2 + H + H_2$	$8.8 \times 10^{-7} \times (T_e/300.0)^{-0.5}$ 1
$CH_5^+ + e^-$	→	$CH_3 + H + H$	$2.2 \times 10^{-7} \times (T_e/300.0)^{-0.5}$ 1
$C_2^+ + e^-$	→	C + C	$3.0 \times 10^{-7} \times (T_e/300.0)^{-0.5}$ 1
$C_2H^+ + e^-$	→	$C_2 + H$	$2.7 \times 10^{-7} \times (T_e/300.0)^{-0.5}$ 1
$C_2H^+ + e^-$	→	CH + C	$2.7 \times 10^{-7} \times (T_e/300.0)^{-0.5}$ 1
$C_2H_2^+ + e^-$	→	$C_2H + H$	$2.7 \times 10^{-7} \times (T_e/300.0)^{-0.5}$ 1
$C_2H_2^+ + e^-$	→	CH + CH	$2.7 \times 10^{-7} \times (T_e/300.0)^{-0.5}$ 1
$C_2H_3^+ + e^-$	→	$C_2H_2 + H$	$4.5 \times 10^{-7} \times (T_e/300.0)^{-0.5}$ 1
$C_2H_3^+ + e^-$	→	$CH_2 + CH$	$4.5 \times 10^{-7} \times (T_e/300.0)^{-0.5}$ 1
$C_2H_4^+ + e^-$	→	$C_2H_3 + H$	$3.0 \times 10^{-7} \times (T_e/300.0)^{-0.5}$ 1
$C_2H_4^+ + e^-$	→	$CH_2 + CH_2$	$3.0 \times 10^{-7} \times (T_e/300.0)^{-0.5}$ 1
$C_2H_5^+ + e^-$	→	$C_2H_4 + H$	$7.4 \times 10^{-7} \times (T_e/300.0)^{-0.5}$ 1
$C_2H_5^+ + e^-$	→	$CH_3 + CH_2$	$7.4 \times 10^{-7} \times (T_e/300.0)^{-0.5}$ 1
$C_2H_6^+ + e^-$	→	$C_2H_5 + H$	$3.0 \times 10^{-7} \times (T_e/300.0)^{-0.5}$ 1
$C_2H_6^+ + e^-$	→	$CH_3 + CH_3$	$3.0 \times 10^{-7} \times (T_e/300.0)^{-0.5}$ 1
$C_2H_7^+ + e^-$	→	$C_2H_6 + H$	$3.5 \times 10^{-7} \times (T_e/300.0)^{-0.5}$ 1
$C_3H^+ + e^-$	→	products	$7.5 \times 10^{-7} \times (T_e/300.0)^{-0.5}$ 1
$C_3H_2^+ + e^-$	→	products	$7.5 \times 10^{-7} \times (T_e/300.0)^{-0.5}$ 1
$C_3H_3^+ + e^-$	→	products	$7.5 \times 10^{-7} \times (T_e/300.0)^{-0.5}$ 1
$C_3H_4^+ + e^-$	→	products	$7.5 \times 10^{-7} \times (T_e/300.0)^{-0.5}$ 1
$C_3H_5^+ + e^-$	→	products	$7.5 \times 10^{-7} \times (T_e/300.0)^{-0.5}$ 1
$C_3H_6^+ + e^-$	→	products	$7.5 \times 10^{-7} \times (T_e/300.0)^{-0.5}$ 1
$C_3H_7^+ + e^-$	→	products	$7.5 \times 10^{-7} \times (T_e/300.0)^{-0.5}$ 1
$C_3H_8^+ + e^-$	→	products	$7.5 \times 10^{-7} \times (T_e/300.0)^{-0.5}$ 1
$C_3H_9^+ + e^-$	→	products	$7.5 \times 10^{-7} \times (T_e/300.0)^{-0.5}$ 1
$C_4H^+ + e^-$	→	products	$7.5 \times 10^{-7} \times (T_e/300.0)^{-0.5}$ 1
$C_4H_2^+ + e^-$	→	products	$7.5 \times 10^{-7} \times (T_e/300.0)^{-0.5}$ 1
$C_4H_3^+ + e^-$	→	products	$7.5 \times 10^{-7} \times (T_e/300.0)^{-0.5}$ 1

Table A1
Continued

Reaction		Rate coefficient	Reference	
$C_4H_5^+ + e^-$	→	products	$7.5 \times 10^{-7} \times (T_e/300.0)^{-0.5}$	1
$C_4H_7^+ + e^-$	→	products	$7.5 \times 10^{-7} \times (T_e/300.0)^{-0.5}$	1
$C_4H_9^+ + e^-$	→	products	$7.5 \times 10^{-7} \times (T_e/300.0)^{-0.5}$	1
$H_2^+ + H_2$	→	$H_3^+ + H$	2.00×10^{-9}	1
$H_2^+ + H$	→	$H^+ + H_2$	6.40×10^{-10}	1
$H_2^+ + He$	→	$HeH^+ + H$	1.40×10^{-10}	1
$H_2^+ + CH_4$	→	$CH_5^+ + H$	1.10×10^{-10}	1
$H_2^+ + CH_4$	→	$CH_4^+ + H_2$	1.41×10^{-9}	1
$H_2^+ + CH_4$	→	$CH_3^+ + H + H_2$	2.28×10^{-9}	1
$H_2^+ + C_2H_2$	→	$C_2H_3^+ + H$	4.77×10^{-10}	1
$H_2^+ + C_2H_2$	→	$C_2H_2^+ + H_2$	4.82×10^{-9}	1
$H_2^+ + C_2H_6$	→	$C_2H_6^+ + H_2$	2.94×10^{-10}	1
$H_2^+ + C_2H_6$	→	$C_2H_5^+ + H + H_2$	1.37×10^{-9}	1
$H_2^+ + C_2H_6$	→	$C_2H_4^+ + H_2 + H_2$	2.35×10^{-9}	1
$H_2^+ + C_2H_6$	→	$C_2H_3^+ + H + H_2 + H_2$	6.86×10^{-10}	1
$H_2^+ + C_2H_6$	→	$C_2H_2^+ + H_2 + H_2 + H_2$	1.96×10^{-10}	1
$He^+ + H_2$	→	$H_2^+ + He$	9.35×10^{-15}	1
$He^+ + H_2$	→	$H^+ + H + He$	4.57×10^{-14}	1
$He^+ + H_2 (\nu \geq 2)$	→	$H^+ + H + He$	1.0×10^{-9}	1
$He^+ + CH_4$	→	$H^+ + CH_3 + He$	4.76×10^{-10}	1
$He^+ + CH_4$	→	$CH^+ + H_2 + H + He$	2.38×10^{-10}	1
$He^+ + CH_4$	→	$CH_2^+ + H_2 + He$	8.50×10^{-10}	1
$He^+ + CH_4$	→	$CH_3^+ + H + He$	8.50×10^{-11}	1
$He^+ + CH_4$	→	$CH_4^+ + He$	5.10×10^{-11}	1
$He^+ + C_2H_2$	→	$C_2H_2^+ + He$	2.45×10^{-10}	1
$He^+ + C_2H_2$	→	$C_2H^+ + H + He$	8.75×10^{-10}	1
$He^+ + C_2H_2$	→	$C_2^+ + H_2 + He$	1.61×10^{-9}	1
$He^+ + C_2H_2$	→	$CH^+ + CH + He$	7.70×10^{-10}	1
$He^+ + C_2H_4$	→	$C_2H_4^+ + He$	2.38×10^{-10}	1
$He^+ + C_2H_4$	→	$C_2H_3^+ + H + He$	1.70×10^{-10}	1
$He^+ + C_2H_4$	→	$C_2H_2^+ + H_2 + He$	2.18×10^{-9}	1
$He^+ + C_2H_4$	→	$C_2H^+ + H + H_2 + He$	4.42×10^{-10}	1
$He^+ + C_2H_4$	→	$CH_2^+ + CH_2 + He$	4.08×10^{-10}	1
$He^+ + C_2H_6$	→	$C_2H_4^+ + H_2 + He$	4.20×10^{-10}	1
$He^+ + C_2H_6$	→	$C_2H_3^+ + H + H_2 + He$	1.74×10^{-9}	1
$He^+ + C_2H_6$	→	$C_2H_2^+ + H_2 + H_2 + He$	8.40×10^{-10}	1
$H^+ + CH_4$	→	$CH_3^+ + H_2$	3.69×10^{-9}	1
$H^+ + CH_4$	→	$CH_4^+ + H$	0.81×10^{-9}	1
$H^+ + C_2H_6$	→	$C_2H_3^+ + H_2 + H_2$	1.30×10^{-9}	1
$H^+ + C_2H_6$	→	$C_2H_4^+ + H + H_2$	1.30×10^{-9}	1
$H^+ + C_2H_6$	→	$C_2H_5^+ + H_2$	1.30×10^{-9}	1
$H^+ + H_2 (\nu \geq 4)$	→	$H_2^+ + H$	2.0×10^{-9}	1
$HeH^+ + H_2$	→	$H_3^+ + He$	1.50×10^{-9}	1

Table A1
Continued

Reaction		Rate coefficient	Reference
HeH ⁺ + H	→	H ₂ ⁺ + He	9.10 × 10 ⁻¹⁰ 1
HeH ⁺ + C ₂ H ₄	→	C ₂ H ₄ ⁺ + H + He	7.00 × 10 ⁻¹⁰ 1
HeH ⁺ + C ₂ H ₄	→	C ₂ H ₃ ⁺ + H ₂ + He	2.10 × 10 ⁻⁹ 1
HeH ⁺ + C ₂ H ₆	→	C ₂ H ₃ ⁺ + H ₂ + H ₂ + He	1.05 × 10 ⁻⁹ 1
HeH ⁺ + C ₂ H ₆	→	C ₂ H ₅ ⁺ + H ₂ + He	1.05 × 10 ⁻⁹ 1
H ₃ ⁺ + CH ₄	→	CH ₅ ⁺ + H ₂	2.40 × 10 ⁻⁹ 1
H ₃ ⁺ + C ₂ H ₂	→	C ₂ H ₃ ⁺ + H ₂	2.90 × 10 ⁻⁹ 1
H ₃ ⁺ + C ₂ H ₄	→	C ₂ H ₅ ⁺ + H ₂	0.69 × 10 ⁻⁹ 1
H ₃ ⁺ + C ₂ H ₄	→	C ₂ H ₃ ⁺ + H ₂ + H ₂	1.61 × 10 ⁻⁹ 1
H ₃ ⁺ + C ₂ H ₆	→	C ₂ H ₅ ⁺ + H ₂ + H ₂	2.40 × 10 ⁻⁹ 1
C ⁺ + CH ₄	→	C ₂ H ₂ ⁺ + H ₂	3.30 × 10 ⁻¹⁰ 1
C ⁺ + CH ₄	→	C ₂ H ₃ ⁺ + H	9.80 × 10 ⁻¹⁰ 1
C ⁺ + C ₂ H ₂	→	C ₃ H ⁺ + H	2.80 × 10 ⁻⁹ 1
C ⁺ + C ₂ H ₄	→	C ₂ H ₃ ⁺ + CH	8.50 × 10 ⁻¹¹ 1
C ⁺ + C ₂ H ₄	→	C ₂ H ₄ ⁺ + C	1.70 × 10 ⁻¹⁰ 1
C ⁺ + C ₂ H ₄	→	C ₃ H ⁺ + H + H ₂	8.50 × 10 ⁻¹¹ 1
C ⁺ + C ₂ H ₄	→	C ₃ H ₂ ⁺ + H ₂	3.40 × 10 ⁻¹⁰ 1
C ⁺ + C ₂ H ₄	→	C ₃ H ₃ ⁺ + H	1.00 × 10 ⁻⁹ 1
C ⁺ + C ₂ H ₆	→	C ₂ H ₂ ⁺ + CH ₄	1.70 × 10 ⁻¹⁰ 1
C ⁺ + C ₂ H ₆	→	C ₂ H ₃ ⁺ + CH ₃	5.10 × 10 ⁻¹⁰ 1
C ⁺ + C ₂ H ₆	→	C ₂ H ₅ ⁺ + CH	1.70 × 10 ⁻¹⁰ 1
C ⁺ + C ₂ H ₆	→	C ₃ H ₃ ⁺ + H + H ₂	8.50 × 10 ⁻¹⁰ 1
CH ⁺ + H	→	C ⁺ + H ₂	7.50 × 10 ⁻¹⁰ 1
CH ⁺ + H ₂	→	CH ₂ ⁺ + H	1.20 × 10 ⁻⁹ 1
CH ⁺ + CH ₄	→	C ₂ H ₄ ⁺ + H	6.50 × 10 ⁻¹¹ 1
CH ⁺ + CH ₄	→	C ₂ H ₃ ⁺ + H ₂	1.10 × 10 ⁻⁹ 1
CH ⁺ + CH ₄	→	C ₂ H ₂ ⁺ + H + H ₂	1.40 × 10 ⁻¹⁰ 1
CH ⁺ + C ₂ H ₂	→	C ₃ H ₂ ⁺ + H	2.40 × 10 ⁻⁹ 1
CH ₂ ⁺ + H ₂	→	CH ₃ ⁺ + H	1.60 × 10 ⁻⁹ 1
CH ₂ ⁺ + CH ₄	→	C ₂ H ₅ ⁺ + H	3.60 × 10 ⁻¹⁰ 1
CH ₂ ⁺ + CH ₄	→	C ₂ H ₄ ⁺ + H ₂	8.40 × 10 ⁻¹⁰ 1
CH ₂ ⁺ + C ₂ H ₂	→	C ₃ H ₃ ⁺ + H	2.50 × 10 ⁻⁹ 1
CH ₃ ⁺ + CH ₄	→	C ₂ H ₅ ⁺ + H ₂	1.20 × 10 ⁻⁹ 1
CH ₃ ⁺ + C ₂ H ₂	→	C ₃ H ₃ ⁺ + H ₂	1.20 × 10 ⁻⁹ 1
CH ₃ ⁺ + C ₂ H ₄	→	C ₂ H ₃ ⁺ + CH ₄	3.50 × 10 ⁻¹⁰ 1
CH ₃ ⁺ + C ₂ H ₄	→	C ₃ H ₃ ⁺ + H ₂ + H ₂	4.60 × 10 ⁻¹¹ 1
CH ₃ ⁺ + C ₂ H ₄	→	C ₃ H ₅ ⁺ + H ₂	5.20 × 10 ⁻¹⁰ 1
CH ₃ ⁺ + C ₂ H ₆	→	C ₂ H ₅ ⁺ + CH ₄	1.50 × 10 ⁻⁹ 1
CH ₃ ⁺ + C ₂ H ₆	→	C ₃ H ₅ ⁺ + H ₂ + H ₂	1.60 × 10 ⁻¹⁰ 1
CH ₃ ⁺ + C ₂ H ₆	→	C ₃ H ₇ ⁺ + H ₂	1.00 × 10 ⁻¹⁰ 1
CH ₄ ⁺ + H ₂	→	CH ₅ ⁺ + H	3.0 × 10 ⁻¹¹ 1
CH ₄ ⁺ + CH ₄	→	CH ₅ ⁺ + CH ₃	1.50 × 10 ⁻⁹ 1
CH ₄ ⁺ + C ₂ H ₂	→	C ₂ H ₂ ⁺ + CH ₄	1.13 × 10 ⁻⁹ 1

Table A1
Continued

Reaction			Rate coefficient	Reference
CH ₄ ⁺ + C ₂ H ₂	→	C ₂ H ₃ ⁺ + CH ₃	1.23 × 10 ⁻⁹	1
CH ₄ ⁺ + C ₂ H ₂	→	C ₃ H ₃ ⁺ + H + H ₂	1.51 × 10 ⁻¹⁰	1
CH ₄ ⁺ + C ₂ H ₄	→	C ₂ H ₄ ⁺ + CH ₄	1.38 × 10 ⁻⁹	1
CH ₄ ⁺ + C ₂ H ₄	→	C ₂ H ₅ ⁺ + CH ₃	4.23 × 10 ⁻¹⁰	1
CH ₄ ⁺ + C ₂ H ₄	→	C ₃ H ₅ ⁺ + H + H ₂	5.52 × 10 ⁻¹¹	1
CH ₄ ⁺ + C ₂ H ₆	→	C ₂ H ₄ ⁺ + CH ₄ + H ₂	1.91 × 10 ⁻⁹	1
CH ₅ ⁺ + H	→	CH ₄ ⁺ + H ₂	1.50 × 10 ⁻¹⁰	1
CH ₅ ⁺ + C ₂ H ₂	→	C ₂ H ₃ ⁺ + CH ₄	1.56 × 10 ⁻⁹	1
CH ₅ ⁺ + C ₂ H ₄	→	C ₂ H ₅ ⁺ + CH ₄	1.50 × 10 ⁻⁹	1
CH ₅ ⁺ + C ₂ H ₆	→	C ₂ H ₅ ⁺ + CH ₄ + H ₂	2.25 × 10 ⁻¹⁰	1
CH ₅ ⁺ + C ₂ H ₆	→	C ₂ H ₇ ⁺ + CH ₄	1.28 × 10 ⁻⁹	1
C ₂ ⁺ + H ₂	→	C ₂ H ⁺ + H	1.20 × 10 ⁻⁹	1
C ₂ ⁺ + CH ₄	→	C ₂ H ⁺ + CH ₃	2.38 × 10 ⁻¹⁰	1
C ₂ ⁺ + CH ₄	→	C ₂ H ₂ ⁺ + CH ₂	1.82 × 10 ⁻¹⁰	1
C ₂ ⁺ + CH ₄	→	C ₃ H ⁺ + H + H ₂	1.96 × 10 ⁻¹⁰	1
C ₂ ⁺ + CH ₄	→	C ₃ H ₂ ⁺ + H ₂	5.74 × 10 ⁻¹⁰	1
C ₂ ⁺ + CH ₄	→	C ₃ H ₃ ⁺ + H	2.10 × 10 ⁻¹⁰	1
C ₂ ⁺ + C ₂ H ₂	→	C ₄ H ⁺ + H	1.20 × 10 ⁻⁹	1
C ₂ ⁺ + C ₂ H ₄	→	products	1.90 × 10 ⁻⁹	1
C ₂ H ⁺ + H ₂	→	C ₂ H ₂ ⁺ + H	1.70 × 10 ⁻⁹	1
C ₂ H ⁺ + CH ₄	→	C ₂ H ₂ ⁺ + CH ₃	3.74 × 10 ⁻¹⁰	1
C ₂ H ⁺ + CH ₄	→	C ₃ H ₃ ⁺ + H ₂	3.74 × 10 ⁻¹⁰	1
C ₂ H ⁺ + CH ₄	→	C ₃ H ₄ ⁺ + H	1.32 × 10 ⁻¹⁰	1
C ₂ H ⁺ + CH ₄	→	C ₃ H ₅ ⁺	2.20 × 10 ⁻¹⁰	1
C ₂ H ⁺ + C ₂ H ₂	→	C ₄ H ₂ ⁺ + H	1.20 × 10 ⁻⁹	1
C ₂ H ⁺ + C ₂ H ₄	→	products	1.71 × 10 ⁻⁹	1
C ₂ H ₂ ⁺ + H ₂	→	C ₂ H ₃ ⁺ + H	1.80 × 10 ⁻¹²	1
C ₂ H ₂ ⁺ + CH ₄	→	C ₃ H ₄ ⁺ + H ₂	1.60 × 10 ⁻¹⁰	1
C ₂ H ₂ ⁺ + CH ₄	→	C ₃ H ₅ ⁺ + H	6.40 × 10 ⁻¹⁰	1
C ₂ H ₂ ⁺ + C ₂ H ₂	→	C ₄ H ₂ ⁺ + H ₂	5.16 × 10 ⁻¹⁰	1
C ₂ H ₂ ⁺ + C ₂ H ₂	→	C ₄ H ₃ ⁺ + H	5.88 × 10 ⁻¹⁰	1
C ₂ H ₂ ⁺ + C ₂ H ₄	→	C ₂ H ₄ ⁺ + C ₂ H ₂	8.96 × 10 ⁻¹⁰	1
C ₂ H ₂ ⁺ + C ₂ H ₄	→	C ₃ H ₃ ⁺ + CH ₃	2.80 × 10 ⁻¹⁰	1
C ₂ H ₂ ⁺ + C ₂ H ₄	→	C ₄ H ₅ ⁺ + H	2.24 × 10 ⁻¹⁰	1
C ₂ H ₂ ⁺ + C ₂ H ₆	→	C ₂ H ₄ ⁺ + C ₂ H ₄	2.63 × 10 ⁻¹⁰	1
C ₂ H ₂ ⁺ + C ₂ H ₆	→	C ₂ H ₅ ⁺ + C ₂ H ₃	1.31 × 10 ⁻¹⁰	1
C ₂ H ₂ ⁺ + C ₂ H ₆	→	C ₃ H ₃ ⁺ + CH ₃ + H ₂	8.76 × 10 ⁻¹¹	1
C ₂ H ₂ ⁺ + C ₂ H ₆	→	C ₃ H ₄ ⁺ + CH ₄	1.46 × 10 ⁻¹¹	1
C ₂ H ₂ ⁺ + C ₂ H ₆	→	C ₃ H ₅ ⁺ + CH ₃	7.88 × 10 ⁻¹⁰	1
C ₂ H ₂ ⁺ + C ₂ H ₆	→	C ₄ H ₅ ⁺ + H + H ₂	7.30 × 10 ⁻¹¹	1
C ₂ H ₂ ⁺ + C ₂ H ₆	→	C ₄ H ₇ ⁺ + H	1.31 × 10 ⁻¹⁰	1
C ₂ H ₃ ⁺ + H	→	C ₂ H ₂ ⁺ + H ₂	1.00 × 10 ⁻¹⁰	1
C ₂ H ₃ ⁺ + CH ₄	→	C ₃ H ₅ ⁺ + H ₂	2.00 × 10 ⁻¹⁰	1

Table A1
Continued

Reaction			Rate coefficient	Reference
$C_2H_3^+ + C_2H_2$	→	$C_4H_3^+ + H_2$	2.16×10^{-10}	1
$C_2H_3^+ + C_2H_4$	→	$C_2H_5^+ + C_2H_2$	9.30×10^{-10}	1
$C_2H_3^+ + C_2H_6$	→	$C_2H_5^+ + C_2H_4$	2.91×10^{-10}	1
$C_2H_3^+ + C_2H_6$	→	$C_3H_5^+ + CH_4$	2.48×10^{-10}	1
$C_2H_3^+ + C_2H_6$	→	$C_4H_7^+ + H_2$	8.06×10^{-11}	1
$C_2H_4^+ + H$	→	$C_2H_3^+ + H_2$	3.0×10^{-10}	1
$C_2H_4^+ + C_2H_2$	→	$C_3H_3^+ + CH_3$	6.73×10^{-10}	1
$C_2H_4^+ + C_2H_2$	→	$C_4H_5^+ + H$	2.37×10^{-10}	1
$C_2H_4^+ + C_2H_4$	→	$C_3H_5^+ + CH_3$	7.19×10^{-10}	1
$C_2H_4^+ + C_2H_4$	→	$C_4H_7^+ + H$	7.11×10^{-11}	1
$C_2H_4^+ + C_2H_6$	→	$C_3H_6^+ + CH_4$	3.71×10^{-13}	1
$C_2H_4^+ + C_2H_6$	→	$C_3H_7^+ + CH_3$	4.93×10^{-12}	1
$C_2H_5^+ + H$	→	$C_2H_4^+ + H_2$	1.0×10^{-11}	1
$C_2H_5^+ + CH_4$	→	$C_3H_7^+ + H_2$	4.00×10^{-15}	1
$C_2H_5^+ + C_2H_2$	→	$C_3H_3^+ + CH_4$	6.84×10^{-11}	1
$C_2H_5^+ + C_2H_2$	→	$C_4H_5^+ + H_2$	1.22×10^{-10}	1
$C_2H_5^+ + C_2H_4$	→	$C_3H_5^+ + CH_4$	3.90×10^{-10}	1
$C_2H_5^+ + C_2H_6$	→	$C_4H_9^+ + H_2$	4.00×10^{-11}	1
$C_2H_6^+ + H$	→	$C_2H_5^+ + H_2$	1.0×10^{-10}	1
$C_2H_6^+ + C_2H_2$	→	$C_2H_5^+ + C_2H_3$	2.22×10^{-10}	1
$C_2H_6^+ + C_2H_2$	→	$C_3H_5^+ + CH_3$	8.19×10^{-10}	1
$C_2H_6^+ + C_2H_2$	→	$C_4H_7^+ + H$	1.29×10^{-10}	1
$C_2H_6^+ + C_2H_4$	→	$C_2H_4^+ + C_2H_6$	1.15×10^{-9}	1
$C_2H_6^+ + C_2H_6$	→	$C_3H_8^+ + CH_4$	7.98×10^{-12}	1
$C_2H_6^+ + C_2H_6$	→	$C_3H_9^+ + CH_3$	1.10×10^{-11}	1
$C_2H_7^+ + C_2H_2$	→	$C_2H_3^+ + C_2H_6$	1.0×10^{-9}	1
$C_2H_7^+ + C_2H_4$	→	$C_2H_5^+ + C_2H_6$	1.0×10^{-9}	1
$H^+ + H_2 + H_2$	→	$H_3^+ + H_2$	3.2×10^{-29}	1
$CH_3^+ + H_2 + H_2$	→	$CH_5^+ + H_2$	3.3×10^{-28}	1
$CH_3^+ + H_2 + He$	→	$CH_5^+ + He$	1.1×10^{-28}	1
$C_2H_2^+ + H_2 + He$	→	$C_2H_4^+ + He$	1.2×10^{-27}	1
$H + H + H_2$	→	$H_2 + H_2$	$2.7 \times 10^{-31} \times (T_n/1)^{-0.6}$	2

Note. Chemical reactions listed in this table are taken into account both in Case 1 and in Case 2. References: *calculated by parameterized formula from Hiraki and Tao (2008); a, Schunk and Nagy (2009); b, Souza and Srivastava (1996); c, Ruberti et al. (2013); d, Ibuki et al. (1989); e, Au et al. (1993); 1, Kim and Fox (1994); 2, Perry et al. (1999). T_e and T_n are the electron temperature and the neutral temperature, respectively.

Table A2
Chemical Reaction List Considered in the Photochemical Model for Case 2

Reaction			Rate coefficient	Reference
Meteoroid ablation	→	Na		**
Meteoroid ablation	→	Fe		**
Meteoroid ablation	→	Mg		**
Meteoroid ablation	→	Si		**
Meteoroid ablation	→	Na ⁺ + e ⁻		**
Meteoroid ablation	→	Fe ⁺ + e ⁻		**
Meteoroid ablation	→	Mg ⁺ + e ⁻		**
Meteoroid ablation	→	Si ⁺ + e ⁻		**
Na	→	Condensation	1.0×10^{-5}	3
Fe	→	Condensation	1.0×10^{-5}	3
Mg	→	Condensation	1.0×10^{-5}	3
Si	→	Condensation	1.0×10^{-5}	3
Na + hν	→	Na ⁺ + e ⁻		f
Fe + hν	→	Fe ⁺ + e ⁻		f
Mg + hν	→	Mg ⁺ + e ⁻		f
Si + hν	→	Si ⁺ + e ⁻		f
Na + H + H ₂	→	NaH + H ₂	$1.2 \times 10^{-30} \times (T_n/1.0)^{-0.6}$	4
Na + CH ₃ + H ₂	→	NaCH ₃ + H ₂	$4.0 \times 10^{-25} \times (T_n/1.0)^{-1.8}$	4
Na ⁺ + H ₂ + H ₂	→	NaH ₂ ⁺ + H ₂	$1.6 \times 10^{-30} \times (T_n/80)^{-0.5}$	4
Na ⁺ + CH ₄ + H ₂	→	NaCH ₄ ⁺ + H ₂	$1.5 \times 10^{-28} \times (T_n/80)^{-1.5}$	4
Na ⁺ + C ₂ H ₂ + H ₂	→	NaC ₂ H ₂ ⁺ + H ₂	$1.3 \times 10^{-28} \times (T_n/80)^{-1.0}$	4
Na ⁺ + C ₂ H ₄ + H ₂	→	NaC ₂ H ₄ ⁺ + H ₂	$1.3 \times 10^{-28} \times (T_n/80)^{-1.5}$	4
Na + H ⁺	→	Na ⁺ + H	1.2×10^{-9}	4
Na + H ₃ ⁺	→	Na ⁺ + H + H ₂	1.1×10^{-9}	4
Na + CH ₃ ⁺	→	Na ⁺ + CH ₃	3.4×10^{-9}	4
Na + C ₂ H ₂ ⁺	→	Na ⁺ + C ₂ H ₂	2.7×10^{-9}	4
Na + C ₃ H ⁺	→	Na ⁺ + products	3.0×10^{-9}	4
Na + C ₃ H ₂ ⁺	→	Na ⁺ + products	3.0×10^{-9}	4
Na + C ₃ H ₃ ⁺	→	Na ⁺ + products	3.0×10^{-9}	4
Na + C ₃ H ₄ ⁺	→	Na ⁺ + products	3.0×10^{-9}	4
Na + C ₃ H ₅ ⁺	→	Na ⁺ + products	3.0×10^{-9}	4
Na + C ₃ H ₆ ⁺	→	Na ⁺ + products	3.0×10^{-9}	4
Na + C ₃ H ₇ ⁺	→	Na ⁺ + products	3.0×10^{-9}	4
Na + C ₃ H ₈ ⁺	→	Na ⁺ + products	3.0×10^{-9}	4
Na + C ₃ H ₉ ⁺	→	Na ⁺ + products	3.0×10^{-9}	4
Na + C ₄ H ⁺	→	Na ⁺ + products	3.0×10^{-9}	4
Na + C ₄ H ₂ ⁺	→	Na ⁺ + products	3.0×10^{-9}	4
Na + C ₄ H ₃ ⁺	→	Na ⁺ + products	3.0×10^{-9}	4
Na + C ₄ H ₅ ⁺	→	Na ⁺ + products	3.0×10^{-9}	4
Na + C ₄ H ₇ ⁺	→	Na ⁺ + products	3.0×10^{-9}	4
Na + C ₄ H ₉ ⁺	→	Na ⁺ + products	3.0×10^{-9}	4
Na + Si ⁺	→	Na ⁺ + Si	2.7×10^{-9}	4
NaH + H	→	Na + H ₂	$1.0 \times 10^{-10} \times (T_n/300)^{-0.5}$	4

Table A2
Continued

Reaction			Rate coefficient	Reference
$\text{Na}^+ + \text{e}^-$	\rightarrow	Na	$2.7 \times 10^{-12} \times (T_e/300)^{-0.6}$	4
$\text{NaH}_2^+ + \text{e}^-$	\rightarrow	Na + H ₂	$1.5 \times 10^{-7} \times (T_e/300)^{-0.5}$	4
$\text{NaH}_2^+ + \text{e}^-$	\rightarrow	NaH + H	$1.5 \times 10^{-7} \times (T_e/300)^{-0.5}$	4
$\text{NaCH}_4^+ + \text{e}^-$	\rightarrow	Na + products	$1.5 \times 10^{-7} \times (T_e/300)^{-0.5}$	4
$\text{NaC}_2\text{H}_2^+ + \text{e}^-$	\rightarrow	Na + products	$1.5 \times 10^{-7} \times (T_e/300)^{-0.5}$	4
$\text{NaC}_2\text{H}_4^+ + \text{e}^-$	\rightarrow	Na + products	$1.5 \times 10^{-7} \times (T_e/300)^{-0.5}$	4
$\text{NaCH}_4^+ + \text{e}^-$	\rightarrow	products	$1.5 \times 10^{-7} \times (T_e/300)^{-0.5}$	4
$\text{NaC}_2\text{H}_2^+ + \text{e}^-$	\rightarrow	products	$1.5 \times 10^{-7} \times (T_e/300)^{-0.5}$	4
$\text{NaC}_2\text{H}_4^+ + \text{e}^-$	\rightarrow	products	$1.5 \times 10^{-7} \times (T_e/300)^{-0.5}$	4
$\text{Fe} + \text{H} + \text{H}_2$	\rightarrow	FeH + H ₂	$1.2 \times 10^{-30} \times (T_n/1.0)^{-1.6}$	4
$\text{Fe}^+ + \text{H} + \text{H}_2$	\rightarrow	FeH ⁺ + H ₂	$3.0 \times 10^{-30} \times (T_n/1.0)^{-1.0}$	4
$\text{Fe}^+ + \text{H}_2 + \text{H}_2$	\rightarrow	FeH ₂ ⁺ + H ₂	2.0×10^{-30}	4
$\text{Fe}^+ + \text{CH}_4 + \text{H}_2$	\rightarrow	FeCH ₄ ⁺ + H ₂	$1.1 \times 10^{-29} \times (T_n/294)^{-1.5}$	4
$\text{Fe}^+ + \text{C}_2\text{H}_2 + \text{H}_2$	\rightarrow	FeC ₂ H ₂ ⁺ + H ₂	$1.4 \times 10^{-26} \times (T_n/294)^{-1.0}$	4
$\text{Fe}^+ + \text{C}_2\text{H}_4 + \text{H}_2$	\rightarrow	FeC ₂ H ₄ ⁺ + H ₂	$1.4 \times 10^{-26} \times (T_n/294)^{-1.5}$	4
$\text{Fe}^+ + \text{C}_2\text{H}_6$	\rightarrow	Fe + C ₂ H ₄ ⁺ + H ₂	$1.1 \times 10^{-12} \times (T_n/300)^{-0.6}$	4
$\text{Fe}^+ + \text{Na}$	\rightarrow	Fe + Na ⁺	1.0×10^{-11}	4
$\text{FeH}^+ + \text{H}$	\rightarrow	Fe ⁺ + H ₂	1.8×10^{-9}	4
$\text{FeH}_2^+ + \text{H}$	\rightarrow	FeH ⁺ + H ₂	1.8×10^{-9}	4
$\text{Fe} + \text{H}^+$	\rightarrow	Fe ⁺ + H	7.4×10^{-9}	4
$\text{Fe} + \text{H}_3^+$	\rightarrow	Fe ⁺ + H + H ₂	4.9×10^{-9}	4
$\text{Fe} + \text{C}^+$	\rightarrow	Fe ⁺ + C	2.6×10^{-9}	4
$\text{Fe} + \text{CH}_3^+$	\rightarrow	Fe ⁺ + CH ₃	2.4×10^{-9}	4
$\text{Fe} + \text{C}_2\text{H}_2^+$	\rightarrow	Fe ⁺ + C ₂ H ₂	2.0×10^{-9}	4
$\text{Fe} + \text{C}_3\text{H}^+$	\rightarrow	Fe ⁺ + products	3.0×10^{-9}	4
$\text{Fe} + \text{C}_3\text{H}_2^+$	\rightarrow	Fe ⁺ + products	3.0×10^{-9}	4
$\text{Fe} + \text{C}_3\text{H}_3^+$	\rightarrow	Fe ⁺ + products	3.0×10^{-9}	4
$\text{Fe} + \text{C}_3\text{H}_4^+$	\rightarrow	Fe ⁺ + products	3.0×10^{-9}	4
$\text{Fe} + \text{C}_3\text{H}_5^+$	\rightarrow	Fe ⁺ + products	3.0×10^{-9}	4
$\text{Fe} + \text{C}_3\text{H}_6^+$	\rightarrow	Fe ⁺ + products	3.0×10^{-9}	4
$\text{Fe} + \text{C}_3\text{H}_7^+$	\rightarrow	Fe ⁺ + products	3.0×10^{-9}	4
$\text{Fe} + \text{C}_3\text{H}_8^+$	\rightarrow	Fe ⁺ + products	3.0×10^{-9}	4
$\text{Fe} + \text{C}_3\text{H}_9^+$	\rightarrow	Fe ⁺ + products	3.0×10^{-9}	4
$\text{Fe} + \text{C}_4\text{H}^+$	\rightarrow	Fe ⁺ + products	3.0×10^{-9}	4
$\text{Fe} + \text{C}_4\text{H}_2^+$	\rightarrow	Fe ⁺ + products	3.0×10^{-9}	4
$\text{Fe} + \text{C}_4\text{H}_3^+$	\rightarrow	Fe ⁺ + products	3.0×10^{-9}	4
$\text{Fe} + \text{C}_4\text{H}_5^+$	\rightarrow	Fe ⁺ + products	3.0×10^{-9}	4
$\text{Fe} + \text{C}_4\text{H}_7^+$	\rightarrow	Fe ⁺ + products	3.0×10^{-9}	4
$\text{Fe} + \text{C}_4\text{H}_9^+$	\rightarrow	Fe ⁺ + products	3.0×10^{-9}	4
$\text{Fe} + \text{Si}^+$	\rightarrow	Fe ⁺ + Si	1.9×10^{-9}	4
$\text{FeH} + \text{H}$	\rightarrow	Fe + H ₂	$1.0 \times 10^{-10} \times (T_n/300)^{0.5}$	4
$\text{Fe}^+ + \text{e}^-$	\rightarrow	Fe	$3.7 \times 10^{-12} \times (T_e/300)^{-0.6}$	4
$\text{FeH}^+ + \text{e}^-$	\rightarrow	Fe + H	$3.0 \times 10^{-7} \times (T_e/300)^{-0.5}$	4

Table A2
Continued

Reaction			Rate coefficient	Reference
$\text{FeH}_2^+ + e^-$	\rightarrow	$\text{FeH} + \text{H}$	$1.5 \times 10^{-7} \times (T_e/300)^{-0.5}$	4
$\text{FeH}_2^+ + e^-$	\rightarrow	$\text{Fe} + \text{H}_2$	$1.5 \times 10^{-7} \times (T_e/300)^{-0.5}$	4
$\text{FeCH}_4^+ + e^-$	\rightarrow	$\text{Fe} + \text{products}$	$1.5 \times 10^{-7} \times (T_e/300)^{-0.5}$	4
$\text{FeC}_2\text{H}_2^+ + e^-$	\rightarrow	$\text{Fe} + \text{products}$	$1.5 \times 10^{-7} \times (T_e/300)^{-0.5}$	4
$\text{FeC}_2\text{H}_4^+ + e^-$	\rightarrow	$\text{Fe} + \text{products}$	$1.5 \times 10^{-7} \times (T_e/300)^{-0.5}$	4
$\text{FeCH}_4^+ + e^-$	\rightarrow	products	$1.5 \times 10^{-7} \times (T_e/300)^{-0.5}$	4
$\text{FeC}_2\text{H}_2^+ + e^-$	\rightarrow	products	$1.5 \times 10^{-7} \times (T_e/300)^{-0.5}$	4
$\text{FeC}_2\text{H}_4^+ + e^-$	\rightarrow	products	$1.5 \times 10^{-7} \times (T_e/300)^{-0.5}$	4
$\text{Mg} + \text{H} + \text{H}_2$	\rightarrow	$\text{MgH} + \text{H}_2$	$1.2 \times 10^{-30} \times (T_n/1.0)^{-0.6}$	4
$\text{Mg}^+ + \text{H} + \text{H}_2$	\rightarrow	$\text{MgH}^+ + \text{H}_2$	$3.0 \times 10^{-30} \times (T_n/1.0)^{-1.0}$	4
$\text{Mg}^+ + \text{H}_2 + \text{H}_2$	\rightarrow	$\text{MgH}_2^+ + \text{H}_2$	$1.6 \times 10^{-30} \times (T_n/80.0)^{-0.5}$	4
$\text{Mg}^+ + \text{CH}_4 + \text{H}_2$	\rightarrow	$\text{MgCH}_4^+ + \text{H}_2$	$1.5 \times 10^{-28} \times (T_n/80.0)^{-1.5}$	4
$\text{Mg}^+ + \text{C}_2\text{H}_2 + \text{H}_2$	\rightarrow	$\text{MgC}_2\text{H}_2^+ + \text{H}_2$	$1.3 \times 10^{-28} \times (T_n/80.0)^{-1.0}$	4
$\text{Mg}^+ + \text{C}_2\text{H}_4 + \text{H}_2$	\rightarrow	$\text{MgC}_2\text{H}_4^+ + \text{H}_2$	$1.3 \times 10^{-28} \times (T_n/80.0)^{-1.5}$	4
$\text{Mg}^+ + \text{Na}$	\rightarrow	$\text{Mg} + \text{Na}^+$	1.0×10^{-11}	4
$\text{MgH}^+ + \text{H}$	\rightarrow	$\text{Mg}^+ + \text{H}_2$	1.8×10^{-9}	4
$\text{MgH}_2^+ + \text{H}$	\rightarrow	$\text{MgH}^+ + \text{H}_2$	1.8×10^{-9}	4
$\text{Mg} + \text{H}^+$	\rightarrow	$\text{Mg}^+ + \text{H}$	1.1×10^{-9}	4
$\text{Mg} + \text{H}_3^+$	\rightarrow	$\text{Mg}^+ + \text{H} + \text{H}_2$	1.0×10^{-9}	4
$\text{Mg} + \text{C}^+$	\rightarrow	$\text{Mg}^+ + \text{C}$	1.1×10^{-9}	4
$\text{Mg} + \text{CH}_3^+$	\rightarrow	$\text{Mg}^+ + \text{CH}_3$	3.5×10^{-10}	4
$\text{Mg} + \text{CH}_5^+$	\rightarrow	$\text{Mg}^+ + \text{CH}_4 + \text{H}$	1.4×10^{-9}	4
$\text{Mg} + \text{C}_2\text{H}_2^+$	\rightarrow	$\text{Mg}^+ + \text{C}_2\text{H}_2$	3.0×10^{-9}	4
$\text{Mg} + \text{C}_3\text{H}^+$	\rightarrow	$\text{Mg}^+ + \text{products}$	3.0×10^{-9}	4
$\text{Mg} + \text{C}_3\text{H}_2^+$	\rightarrow	$\text{Mg}^+ + \text{products}$	3.0×10^{-9}	4
$\text{Mg} + \text{C}_3\text{H}_3^+$	\rightarrow	$\text{Mg}^+ + \text{products}$	3.0×10^{-9}	4
$\text{Mg} + \text{C}_3\text{H}_4^+$	\rightarrow	$\text{Mg}^+ + \text{products}$	3.0×10^{-9}	4
$\text{Mg} + \text{C}_3\text{H}_5^+$	\rightarrow	$\text{Mg}^+ + \text{products}$	3.0×10^{-9}	4
$\text{Mg} + \text{C}_3\text{H}_6^+$	\rightarrow	$\text{Mg}^+ + \text{products}$	3.0×10^{-9}	4
$\text{Mg} + \text{C}_3\text{H}_7^+$	\rightarrow	$\text{Mg}^+ + \text{products}$	3.0×10^{-9}	4
$\text{Mg} + \text{C}_3\text{H}_8^+$	\rightarrow	$\text{Mg}^+ + \text{products}$	3.0×10^{-9}	4
$\text{Mg} + \text{C}_3\text{H}_9^+$	\rightarrow	$\text{Mg}^+ + \text{products}$	3.0×10^{-9}	4
$\text{Mg} + \text{C}_4\text{H}^+$	\rightarrow	$\text{Mg}^+ + \text{products}$	3.0×10^{-9}	4
$\text{Mg} + \text{C}_4\text{H}_2^+$	\rightarrow	$\text{Mg}^+ + \text{products}$	3.0×10^{-9}	4
$\text{Mg} + \text{C}_4\text{H}_3^+$	\rightarrow	$\text{Mg}^+ + \text{products}$	3.0×10^{-9}	4
$\text{Mg} + \text{C}_4\text{H}_5^+$	\rightarrow	$\text{Mg}^+ + \text{products}$	3.0×10^{-9}	4
$\text{Mg} + \text{C}_4\text{H}_7^+$	\rightarrow	$\text{Mg}^+ + \text{products}$	3.0×10^{-9}	4
$\text{Mg} + \text{C}_4\text{H}_9^+$	\rightarrow	$\text{Mg}^+ + \text{products}$	3.0×10^{-9}	4
$\text{Mg} + \text{Si}^+$	\rightarrow	$\text{Mg}^+ + \text{Si}$	2.9×10^{-9}	4
$\text{MgH} + \text{H}$	\rightarrow	$\text{Mg} + \text{H}_2$	$1.0 \times 10^{-10} \times (T_n/300)^{0.5}$	4
$\text{Mg}^+ + e^-$	\rightarrow	Mg	$2.8 \times 10^{-12} \times (T_e/300)^{-0.8}$	4
$\text{MgH}^+ + e^-$	\rightarrow	$\text{Mg} + \text{H}$	$3.0 \times 10^{-7} \times (T_e/300)^{-0.5}$	4
$\text{MgH}_2^+ + e^-$	\rightarrow	$\text{Mg} + \text{H}_2$	$1.5 \times 10^{-7} \times (T_e/300)^{-0.5}$	4

Table A2
Continued

Reaction		Rate coefficient	Reference	
$\text{MgH}_2^+ + e^-$	\rightarrow	$\text{MgH} + \text{H}$	$1.5 \times 10^{-7} \times (T_e/300)^{-0.5}$	4
$\text{MgCH}_4^+ + e^-$	\rightarrow	$\text{Mg} + \text{products}$	$1.5 \times 10^{-7} \times (T_e/300)^{-0.5}$	4
$\text{MgC}_2\text{H}_2^+ + e^-$	\rightarrow	$\text{Mg} + \text{products}$	$1.5 \times 10^{-7} \times (T_e/300)^{-0.5}$	4
$\text{MgC}_2\text{H}_4^+ + e^-$	\rightarrow	$\text{Mg} + \text{products}$	$1.5 \times 10^{-7} \times (T_e/300)^{-0.5}$	4
$\text{MgCH}_4^+ + e^-$	\rightarrow	products	$1.5 \times 10^{-7} \times (T_e/300)^{-0.5}$	4
$\text{MgC}_2\text{H}_2^+ + e^-$	\rightarrow	products	$1.5 \times 10^{-7} \times (T_e/300)^{-0.5}$	4
$\text{MgC}_2\text{H}_4^+ + e^-$	\rightarrow	products	$1.5 \times 10^{-7} \times (T_e/300)^{-0.5}$	4
$\text{Si} + \text{H} + \text{H}_2$	\rightarrow	$\text{SiH} + \text{H}_2$	$1.2 \times 10^{-30} \times (T_n/1.0)^{-0.6}$	4
$\text{Si}^+ + \text{H} + \text{H}_2$	\rightarrow	$\text{SiH}^+ + \text{H}_2$	$3.0 \times 10^{-30} \times (T_n/1.0)^{-1.0}$	4
$\text{Si}^+ + \text{H}_2 + \text{H}_2$	\rightarrow	$\text{SiH}_2^+ + \text{H}_2$	$1.6 \times 10^{-30} \times (T_n/80)^{-0.5}$	4
$\text{Si}^+ + \text{CH}_4 + \text{H}_2$	\rightarrow	$\text{SiC}_n\text{H}_m^+ + \text{H}_2$	$1.4 \times 10^{-28} \times (T_n/80)^{-1.5}$	4
$\text{Si}^+ + \text{C}_2\text{H}_2 + \text{H}_2$	\rightarrow	$\text{SiC}_n\text{H}_m^+ + \text{H}_2$	$1.2 \times 10^{-28} \times (T_n/80)^{-1.0}$	4
$\text{Si}^+ + \text{C}_2\text{H}_4 + \text{H}_2$	\rightarrow	$\text{SiC}_n\text{H}_m^+ + \text{H}_2$	$1.2 \times 10^{-28} \times (T_n/80)^{-1.5}$	4
$\text{Si}^+ + \text{H}_2$	\rightarrow	SiH_2^+	3.0×10^{-18}	4
$\text{Si}^+ + \text{CH}_3$	\rightarrow	$\text{SiC}_n\text{H}_m^+ + \text{H}$	1.0×10^{-9}	4
$\text{Si}^+ + \text{CH}_3$	\rightarrow	$\text{SiC}_n\text{H}_m^+ + \text{H}_2$	1.0×10^{-9}	4
$\text{Si}^+ + \text{CH}_4$	\rightarrow	$\text{SiC}_n\text{H}_m^+ + \text{H}$	7.7×10^{-11}	4
$\text{Si}^+ + \text{C}_2\text{H}_2$	\rightarrow	$\text{SiC}_n\text{H}_m^+ + \text{H}$	1.8×10^{-10}	4
$\text{Si}^+ + \text{C}_2\text{H}_4$	\rightarrow	$\text{SiC}_n\text{H}_m^+ + \text{CH}_3 + \text{H}$	7.4×10^{-11}	4
$\text{Si}^+ + \text{C}_2\text{H}_4$	\rightarrow	$\text{SiC}_n\text{H}_m^+ + \text{H}$	1.0×10^{-9}	4
$\text{Si}^+ + \text{C}_2\text{H}_6$	\rightarrow	$\text{SiC}_n\text{H}_m^+ + \text{CH}_4$	1.2×10^{-10}	4
$\text{Si}^+ + \text{C}_2\text{H}_6$	\rightarrow	$\text{SiC}_n\text{H}_m^+ + \text{CH}_3$	6.4×10^{-10}	4
$\text{Si}^+ + \text{C}_2\text{H}_6$	\rightarrow	$\text{SiC}_n\text{H}_m^+ + \text{CH}_3 + \text{H}_2$	2.4×10^{-11}	4
$\text{SiH}^+ + \text{H}$	\rightarrow	$\text{Si}^+ + \text{H}_2$	1.9×10^{-9}	4
$\text{SiH}_2^+ + \text{H}$	\rightarrow	$\text{SiH}^+ + \text{H}_2$	1.8×10^{-9}	4
$\text{Si} + \text{H}^+$	\rightarrow	$\text{Si}^+ + \text{H}$	9.9×10^{-10}	4
$\text{Si} + \text{H}_3^+$	\rightarrow	$\text{SiH}^+ + \text{H}_2$	3.7×10^{-9}	4
$\text{Si} + \text{CH}_3^+$	\rightarrow	$\text{SiC}_n\text{H}_m^+ + \text{H}$	2.0×10^{-9}	4
$\text{Si} + \text{CH}_3^+$	\rightarrow	$\text{SiC}_n\text{H}_m^+ + \text{H}_2$	2.0×10^{-9}	4
$\text{Si} + \text{CH}_5^+$	\rightarrow	$\text{SiC}_n\text{H}_m^+ + \text{H}$	2.0×10^{-10}	4
$\text{Si} + \text{CH}_5^+$	\rightarrow	$\text{SiC}_n\text{H}_m^+ + \text{H}_2$	2.0×10^{-10}	4
$\text{Si} + \text{C}_2\text{H}_3^+$	\rightarrow	$\text{SiC}_n\text{H}_m^+ + \text{H}_2$	2.0×10^{-10}	4
$\text{Si} + \text{C}_2\text{H}_3^+$	\rightarrow	$\text{SiC}_n\text{H}_m^+ + \text{H}$	2.0×10^{-10}	4
$\text{Si} + \text{C}_3\text{H}^+$	\rightarrow	$\text{SiC}_n\text{H}_m^+ + \text{products}$	2.0×10^{-10}	4
$\text{Si} + \text{C}_3\text{H}_2^+$	\rightarrow	$\text{SiC}_n\text{H}_m^+ + \text{products}$	2.0×10^{-10}	4
$\text{Si} + \text{C}_3\text{H}_3^+$	\rightarrow	$\text{SiC}_n\text{H}_m^+ + \text{products}$	2.0×10^{-10}	4
$\text{Si} + \text{C}_3\text{H}_4^+$	\rightarrow	$\text{SiC}_n\text{H}_m^+ + \text{products}$	2.0×10^{-10}	4
$\text{Si} + \text{C}_3\text{H}_5^+$	\rightarrow	$\text{SiC}_n\text{H}_m^+ + \text{products}$	2.0×10^{-10}	4
$\text{Si} + \text{C}_3\text{H}_6^+$	\rightarrow	$\text{SiC}_n\text{H}_m^+ + \text{products}$	2.0×10^{-10}	4
$\text{Si} + \text{C}_3\text{H}_7^+$	\rightarrow	$\text{SiC}_n\text{H}_m^+ + \text{products}$	2.0×10^{-10}	4
$\text{Si} + \text{C}_3\text{H}_8^+$	\rightarrow	$\text{SiC}_n\text{H}_m^+ + \text{products}$	2.0×10^{-10}	4
$\text{Si} + \text{C}_3\text{H}_9^+$	\rightarrow	$\text{SiC}_n\text{H}_m^+ + \text{products}$	2.0×10^{-10}	4
$\text{Si} + \text{C}_4\text{H}^+$	\rightarrow	$\text{SiC}_n\text{H}_m^+ + \text{products}$	2.0×10^{-10}	4

Table A2
Continued

Reaction		Rate coefficient	Reference	
Si + C ₄ H ₂ ⁺	→	SiC _n H _m ⁺ + products	2.0 × 10 ⁻¹⁰	4
Si + C ₄ H ₃ ⁺	→	SiC _n H _m ⁺ + products	2.0 × 10 ⁻¹⁰	4
Si + C ₄ H ₅ ⁺	→	SiC _n H _m ⁺ + products	2.0 × 10 ⁻¹⁰	4
Si + C ₄ H ₇ ⁺	→	SiC _n H _m ⁺ + products	2.0 × 10 ⁻¹⁰	4
Si + C ₄ H ₉ ⁺	→	SiC _n H _m ⁺ + products	2.0 × 10 ⁻¹⁰	4
Si + CH ₂	→	SiCH + H	2.0 × 10 ⁻¹¹ × (T _e /300) ^{-0.5}	4
Si + CH ₃	→	SiCH ₂ + H	4.0 × 10 ⁻¹¹ × (T _e /300) ^{0.5}	4
SiH + H	→	Si + H ₂	1.0 × 10 ⁻¹⁰ × (T _e /300) ^{0.5}	4
Si ⁺ + e ⁻	→	Si	4.9 × 10 ⁻¹² × (T _e /300) ^{-0.6}	4
SiH ⁺ + e ⁻	→	Si + H	2.0 × 10 ⁻⁷ × (T _e /300) ^{-0.5}	4
SiH ₂ ⁺ + e ⁻	→	Si + H + H	2.0 × 10 ⁻⁷ × (T _e /300) ^{-0.5}	4
SiH ₂ ⁺ + e ⁻	→	SiH + H	1.5 × 10 ⁻⁷ × (T _e /300) ^{-0.5}	4
SiH ₂ ⁺ + e ⁻	→	Si + H ₂	1.5 × 10 ⁻⁷ × (T _e /300) ^{-0.5}	4
SiC _n H _m ⁺ + e ⁻	→	Si	1.5 × 10 ⁻⁷ × (T _e /300) ^{-0.5}	4
SiC _n H _m ⁺ + e ⁻	→	products	1.5 × 10 ⁻⁷ × (T _e /300) ^{-0.5}	4

Note. Chemical reactions listed in this table are taken into account only in Case 2. References: **calculated by the meteoroid ablation model; 3, Moses and Bass (2000); f, Verner et al. (1993); 4, Kim et al. (2001). T_e and T_n are the electron temperature and the neutral temperature, respectively.

Data Availability Statement

The modeling data supporting the figures presented in this paper are available at <https://doi.org/10.5281/zenodo.5887630>.

Acknowledgments

This work was supported by JSPS KAKENHI grant numbers JP18H05439 and JP20H00192. Work at NICT (Aoi Nakamizo), Kyushu University (Akimasa Yoshikawa), and JHU/APL (Shinichi Ohtani) was supported by JSPS KAKENHI Grant Number 20H01961. Work at the University of Tokyo (Kazuo Yoshioka) was supported by JSPS KAKENHI Grant Number 19H01948. Work at JHU/APL (Shinichi Ohtani) was supported by National Science Foundation (NSF) grant 1502700. Y. Nakamura is supported by the International Joint Graduate Program in Earth and Environmental Sciences, Tohoku University (GP-EES).

References

- Acuna, M. H., & Ness, N. F. (1976). The main magnetic field of Jupiter. *Journal of Geophysical Research*, 81(16), 2917–2922. <https://doi.org/10.1029/JA081i016p02917>
- Au, J. W., Cooper, G., & Brion, C. E. (1993). The molecular and dissociative photoionization of ethane, propane, and *n*-butane: Absolute oscillator strengths (10–80 eV) and breakdown pathways. *Chemical Physics*, 173, 241–265. [https://doi.org/10.1016/0301-0104\(93\)80143-w](https://doi.org/10.1016/0301-0104(93)80143-w)
- Barrow, D., & Matcheva, K. I. (2011). Impact of atmospheric gravity waves on the Jovian ionosphere. *Icarus*, 211(1), 609–622. <https://doi.org/10.1016/j.icarus.2010.10.017>
- Chapman, S., & Cowling, T. G. (1970). *The mathematical theory of non-uniform gases* (pp. 86–87). Cambridge, UK: Cambridge University Press.
- Connerney, J. E. P., Timmins, S., Oliverson, R. J., Espley, J. R., Joergensen, J. L., Kotsiaros, S., et al. (2022). A new model of Jupiter's magnetic field at the completion of Juno's Prime Mission. *Journal of Geophysical Research: Planets*, 127, e2021JE007055. <https://doi.org/10.1029/2021JE007055>
- Fjeldbo, G., Kliore, A., Seidel, B., Sweetnam, D., & Cain, D. (1975). Pioneer 10 radio occultation measurements of the ionosphere of Jupiter. *Astronomy & Astrophysics*, 39, 91–96.
- Gérard, J.-C., Gkouvelis, L., Bonfond, B., Grodent, D., Gladstone, G. R., Hue, V., et al. (2020). Spatial distribution of the Pedersen conductance in the Jovian aurora from Juno-UVS spectral images. *Journal of Geophysical Research: Space Physics*, 125, e2020JA028142. <https://doi.org/10.1029/2020JA028142>
- Grodent, D., Waite, J. H., Jr., & Gérard, J.-C. (2001). A self-consistent model of the Jovian auroral thermal structure. *Journal of Geophysical Research*, 106(A7), 12933–12952. <https://doi.org/10.1029/2000JA900129>
- Hinson, D. P., Flasar, F. M., Kliore, A. J., Schinder, P. J., Twicken, J. D., & Herrera, R. G. (1997). Jupiter's ionosphere: Results from the first Galileo radio occultation experiment. *Geophysical Research Letters*, 24(17), 2107–2110. <https://doi.org/10.1029/97GL01608>
- Hinson, D. P., Twicken, J. D., & Karayel, E. T. (1998). Jupiter's ionosphere: New results from Voyager 2 radio occultation measurements. *Journal of Geophysical Research*, 103(A5), 9505–9520. <https://doi.org/10.1029/97JA03689>
- Hiraki, Y., & Tao, C. (2008). Parameterization of ionization rate by auroral electron precipitation in Jupiter. *Annales Geophysicae*, 26, 77–86. <https://doi.org/10.5194/angeo-26-77-2008>
- Hughes, D. W. (1978). Meteors. In *Cosmic dust* (pp. 123–185). Chichester, UK/New York: Wiley-Interscience.
- Hughes, D. W. (1993). Meteorite incident angles. *Journal of the British Astronomical Association*, 103(3), 123–126.
- Hunten, D. M. (1973). The escape of light gases from planetary atmospheres. *Journal of the Atmospheric Sciences*, 30(8), 1481–1494. [https://doi.org/10.1175/1520-0469\(1973\)030<1481:TEOLGF>2.0.CO;2](https://doi.org/10.1175/1520-0469(1973)030<1481:TEOLGF>2.0.CO;2)
- Ibuki, T., Cooper, G., & Brion, C. E. (1989). Absolute dipole oscillator strength for photoabsorption and the molecular and dissociative photoionization of ethylene. *Chemical Physics*, 129, 295–309. [https://doi.org/10.1016/0301-0104\(89\)85002-5](https://doi.org/10.1016/0301-0104(89)85002-5)

- Kim, Y. H., & Fox, J. L. (1994). The chemistry of hydrocarbon ions in the Jovian ionosphere. *Icarus*, *112*, 310–325. <https://doi.org/10.1006/icar.1994.1186>
- Kim, Y. H., Pesnell, W. D., Grebowsky, J. M., & Fox, J. L. (2001). Meteoric ions in the ionosphere of Jupiter. *Icarus*, *150*, 261–278. <https://doi.org/10.1006/icar.2001.6590>
- Kivelson, M. G., & Bagenal, F. (2007). Chapter 28—Planetary magnetospheres. In L.-A. McFadden, P. R. Weissman, & T. V. Johnson (Eds.), *Encyclopedia of the solar system* (2nd ed., pp. 519–540). San Diego, CA: Academic Press. <https://doi.org/10.1016/B978-012088589-3/50032-3>
- Lebedinets, V. N., Manochina, A. V., & Shushkova, V. B. (1973). Interaction of the lower thermosphere with the solid component of the interplanetary medium. *Planetary and Space Science*, *21*, 1317–1332. [https://doi.org/10.1016/0032-0633\(73\)90224-9](https://doi.org/10.1016/0032-0633(73)90224-9)
- Lyons, J. R. (1995). Metal ions in the atmosphere of Neptune. *Science*, *267*, 648–651. <https://doi.org/10.1126/science.7839139>
- Majeed, T., & McConnell, J. C. (1991). The upper ionospheres of Jupiter and Saturn. *Planetary and Space Science*, *39*, 1715–1732. [https://doi.org/10.1016/0032-0633\(91\)90031-5](https://doi.org/10.1016/0032-0633(91)90031-5)
- Millward, G., Miller, S., Stallard, T., Aylward, A. D., & Achilleos, N. (2002). On the dynamics of the Jovian ionosphere and thermosphere: III. The modelling of auroral conductivity. *Icarus*, *160*, 95–107. <https://doi.org/10.1006/icar.2002.6951>
- Moses, J. I., & Bass, S. F. (2000). The effects of external material on the chemistry and structure of Saturn's ionosphere. *Journal of Geophysical Research*, *105*(E3), 7013–7052. <https://doi.org/10.1029/1999JE001172>
- Moses, J. I., & Poppe, A. (2017). Dust ablation on the giant planets: Consequences for stratospheric photochemistry. *Icarus*, *297*, 33–58. <https://doi.org/10.1016/j.icarus.2017.06.002>
- Nagy, A. F., Chameides, W. L., Chen, R. H., & Atreya, S. K. (1976). Electron temperatures in the Jovian ionosphere. *Journal of Geophysical Research*, *81*(31), 5567–5569. <https://doi.org/10.1029/JA081i031p05567>
- Nesvorný, D., Jenniskens, P., Levison, H. F., Bottke, W. F., Vokrouhlický, D., & Gounelle, M. (2010). Cometary origin of the zodiacal cloud and carbonaceous micrometeorites. Implications for hot debris disks. *The Astrophysical Journal*, *713*(2), 816–836. <https://doi.org/10.1088/0004-637X/713/2/816>
- Nichols, J. D., & Cowley, S. W. H. (2004). Magnetosphere–ionosphere coupling currents in Jupiter's middle magnetosphere: Effect of precipitation-induced enhancement of the ionospheric Pedersen conductivity. *Annales Geophysicae*, *22*, 1799–1827. <https://doi.org/10.5194/angeo-22-1799-2004>
- Perry, J. J., Kim, Y. H., Fox, J. L., & Porter, H. S. (1999). Chemistry of the Jovian auroral ionosphere. *Journal of Geophysical Research*, *104*(E7), 16541–16565. <https://doi.org/10.1029/1999JE900022>
- Pesnell, W. D., & Grebowsky, J. M. (2000). Meteoric magnesium ions in the Martian atmosphere. *Journal of Geophysical Research*, *105*(E1), 1695–1707. <https://doi.org/10.1029/1999JE001115>
- Plane, J. M. C., Flynn, G. J., Määttä, A., Moores, J. E., Poppe, A. R., Carrillo-Sanchez, J. D., & Listowski, C. (2018). Impacts of cosmic dust on planetary atmospheres and surfaces. *Space Science Reviews*, *214*, 23. <https://doi.org/10.1007/s11214-017-0458-1>
- Poppe, A. R. (2016). An improved model for interplanetary dust fluxes in the outer Solar System. *Icarus*, *264*, 369–386. <https://doi.org/10.1016/j.icarus.2015.10.001>
- Ren, C., & McKenzie, A. R. (2007). Closed-form approximations to the error and complementary error functions and their applications in atmospheric science. *Atmospheric Science Letters*, *8*, 70–73. <https://doi.org/10.1002/asl.154>
- Richards, P. G., Fennelly, J. A., & Torr, D. G. (1994). EUVAC: A solar EUV flux model for aeronomic calculations. *Journal of Geophysical Research*, *99*(A5), 8981–8992. <https://doi.org/10.1029/94JA00518>
- Ruberti, M., Yun, R., Gokhberg, K., Kopelke, S., Cederbaum, L. S., Tarantelli, F., & Averbukh, V. (2013). Total molecular photoionization cross-sections by algebraic diagrammatic construction–Stieltjes–Lanczos method: Benchmark calculations. *The Journal of Chemical Physics*, *139*, 144107. <https://doi.org/10.1063/1.4824431>
- Schunk, R. W., & Nagy, A. F. (2009). *Ionospheres: Physics, plasma physics, and chemistry*. Cambridge: Cambridge University Press. <https://doi.org/10.1017/CBO9780511635342>
- Shinagawa, H., Miyoshi, Y., Jin, H., & Fujiwara, H. (2017). Global distribution of neutral wind shear associated with sporadic E layers derived from GAIA. *Journal of Geophysical Research: Space Physics*, *122*, 4450–4465. <https://doi.org/10.1002/2016JA023778>
- Singhal, R. P. (1996). Hall and Pedersen conductivities in the auroral ionosphere of Jupiter. *Indian Journal of Radio & Space Physics*, *25*, 361–366.
- Smith, C. G. A., Miller, S., & Aylward, A. D. (2005). Magnetospheric energy inputs into the upper atmospheres of the giant planets. *Annales Geophysicae*, *23*, 1943–1947. <https://doi.org/10.5194/angeo-23-1943-2005>
- Smith, F. L., III, & Smith, C. (1972). Numerical evaluation of Chapman's grazing incidence integral $ch(X, \chi)$. *Journal of Geophysical Research*, *77*(19), 3592–3597. <https://doi.org/10.1029/JA077i019p03592>
- Souza, A. C. A., & Srivastava, S. K. (1996). Photoabsorption cross sections derived by the electron energy loss spectroscopy technique for ammonia, methane and acetylene in the photon energy range of 5 to 100 eV. *Journal of the Brazilian Chemical Society*, *7*, 91–95. <https://doi.org/10.5935/0103-5053.19960012>
- Tao, C., Fujiwara, H., & Kasaba, Y. (2009). Neutral wind control of the Jovian magnetosphere–ionosphere current system. *Journal of Geophysical Research*, *114*, A08307. <https://doi.org/10.1029/2008JA013966>
- Tao, C., Fujiwara, H., & Kasaba, Y. (2010). Jovian magnetosphere–ionosphere current system characterized by diurnal variation of ionospheric conductance. *Planetary and Space Science*, *58*(3), 351–364. <https://doi.org/10.1016/j.pss.2009.10.005>
- Verner, D. A., Yakovlev, D. G., Band, I. M., & Trzhaskovskaya, M. B. (1993). Subshell photoionization cross sections and ionization energies of atoms and ions from He to Zn. *Atomic Data and Nuclear Data Tables*, *55*(2), 233–280. <https://doi.org/10.1006/adnd.1993.1022>
- Vondrak, T., Plane, J. M. C., Broadley, S., & Janches, D. (2008). A chemical model of meteoric ablation. *Atmospheric Chemistry and Physics*, *8*, 7015–7031. <https://doi.org/10.5194/acp-8-7015-2008>